HHS Public Access

Author manuscript

Neuron. Author manuscript; available in PMC 2021 December 02.

Published in final edited form as:

Neuron. 2019 April 17; 102(2): 477–492.e5. doi:10.1016/j.neuron.2019.02.010.

Higher-Order Thalamic Circuits Channel Parallel Streams of Visual Information in Mice

Corbett Bennett[1,3], **Samuel D. Gale**[1,3,4,*], **Marina E. Garrett**[1,2], **Melissa L. Newton**[2], **Edward M. Callaway**[2], **Gabe J. Murphy**[1], **Shawn R. Olsen**[1]

[1]Allen Institute for Brain Science, 615 Westlake Avenue, Seattle, WA 98109, USA

[2]Systems Neurobiology Laboratories, The Salk Institute for Biological Studies, 10010 North Torrey Pines Road, La Jolla, CA 92037, USA

[3]These authors contributed equally

[4]Lead Contact

SUMMARY

Higher-order thalamic nuclei, such as the visual pulvinar, play essential roles in cortical function by connecting functionally related cortical and subcortical brain regions. A coherent framework describing pulvinar function remains elusive because of its anatomical complexity and involvement in diverse cognitive processes. We combined large-scale anatomical circuit mapping with high-density electrophysiological recordings to dissect a homolog of the pulvinar in mice, the lateral posterior thalamic nucleus (LP). We define three broad LP subregions based on correspondence between connectivity and functional properties. These subregions form corticothalamic loops biased toward ventral or dorsal stream cortical areas and contain separate representations of visual space. Silencing the visual cortex or superior colliculus revealed that they drive visual tuning properties in separate LP subregions. Thus, by specifying the driving input sources, functional properties, and downstream targets of LP circuits, our data provide a roadmap for understanding the mechanisms of higher-order thalamic function in vision.

In Brief

Bennett et al. divide the mouse pulvinar (LP) into 3 subregions with distinct anatomical connections and functional properties. They find that the superior colliculus conveys object motion to ventral stream cortical areas via posterior LP, whereas anterior LP targets dorsal stream areas.

*Correspondence: samg@alleninstitute.org.

AUTHOR CONTRIBUTIONS

C.B. and S.D.G. conceived the project, performed experiments, analyzed data, and wrote the manuscript. M.E.G. and M.L.N. performed the rabies tracing experiments under E.M.C.'s supervision. S.R.O. supervised C.B. and S.D.G. and helped write the manuscript. G.J.M. helped conceive the project. All authors contributed to editing the manuscript.

DECLARATION OF INTERESTS

The authors declare no competing interests.

SUPPLEMENTAL INFORMATION

Supplemental Information includes eight figures and three tables and can be found with this article online at https://doi.org/10.1016/j.neuron.2019.02.010.

INTRODUCTION

The higher-order thalamus is critically involved in cortical function, both as a route by which cortical areas communicate and as a relay of subcortical input to the cortex. The pulvinar, the higher-order thalamic nucleus in the visual system, is reciprocally connected with multiple visual and frontal cortical areas and, therefore, mediates an indirect pathway for cortico-cortical communication through cortico-thalamo-cortical ("transthalamic") circuits (Sherman, 2016). The pulvinar also receives a dense projection from the superficial (retino-recipient) layers of the superior colliculus (SCs), which interacts with transthalamic circuits, potentially forming a secondary route of information flow from the retina to the cortex that runs parallel to the retino-geniculate pathway. The relative contributions of cortical and SCs input in driving pulvinar visual responses and the information these pathways carry remain uncertain.

The lateral posterior thalamic nucleus (LP) in rodents is thought to be homologous to the primate visual pulvinar (Baldwin et al., 2017). Like the pulvinar, mouse LP is reciprocally connected with all visual cortical areas and receives a strong projection from the SCs (Oh et al., 2014; Tohmi et al., 2014; Zhou et al., 2017). Previous studies have divided LP into subregions based on cytoarchitecture and immunocytochemical markers (Nakamura et al., 2015; Takahashi, 1985; Zhou et al., 2017), but it is unclear whether these subregions reflect functionally distinct domains of LP. Conversely, functional studies have shown that LP neurons encode a variety of sensory and motor signals and convey these to the visual cortex (Allen et al., 2016; Durand et al., 2016; Roth et al., 2016), but these studies focused on limited portions of LP and did not relate functional differences to LP anatomy. Moreover, none of these studies tested the causal role of cortical or SC input in driving LP visual responses.

Here we performed comprehensive anatomical input-output mapping and high-density electrophysiological recordings across the full extent of LP to elucidate the relationship between structural and functional organization in the mouse corticothalamic visual system. We found that LP is not a homogeneous structure; rather, we identified three subregions with different patterns of connectivity with visual cortical areas, frontal cortex, and SC. To test whether these regions differentially depend on the retino-SC or retino-geniculate-V1 pathways, we silenced either SC or primary visual cortex (V1). We found that SC input drives visual responses to object motion in posterior LP. Interestingly, unlike in primates (Kaas and Lyon, 2007), this information is routed primarily to ventral stream rather than dorsal stream visual cortical areas. In contrast, visual responses in anterior LP are driven by V1 input and are primarily routed to dorsal stream visual cortical areas. Together, these data show a tight correspondence between anatomical, functional, and perturbational maps of LP and reveal that SC is the main driver of activity in a thalamo-cortical circuit linking LP to primarily ventral stream visual areas.

RESULTS

Anatomical Input Mapping Divides LP into Three Broad Subregions

LP activity is shaped by input from diverse cortical and subcortical structures. Functionally relevant subregions of LP might therefore be defined by distinct patterns of input connections. To generate detailed maps of LP input connectivity, we quantified axon labeling in LP resulting from anterograde viral tracer injections into SCs, eight visual cortical areas, and two frontal cortical areas (Figure 1A; all injections taken from the Allen Mouse Brain Connectivity Database). Axonal projections were mapped to a standardized anatomical coordinate system for comparison (the Allen Mouse Common Coordinate Framework [CCF]), yielding an “input volume” for each source area, representing which LP voxels are targeted by axons from that area.

Visual inspection of LP input volumes revealed two general principles of LP organization. First, SCs axons projected densely to the posterior half of LP but were sparse in anterior regions, whereas input from frontal areas (anterior cingulate [ACA] and orbital cortex [ORB]) was confined almost exclusively to medial LP. Second, input from visual cortical areas was overlapping but organized so that axons from ventral stream areas tended to aggregate in posterior and dorsal LP with SCs axons, whereas axons from dorsal stream areas were biased toward anterior and ventral LP along with V1 axons (Figure 1A).

To quantify the degree to which axons from different source regions overlap in LP, we computed the normalized dot product between each input volume (Figure 1B). The resulting similarity matrix confirmed our qualitative observations and suggested that specific groups of input sources primarily target different regions of LP. To further quantify these relationships, we clustered LP voxels based on their input (Figures 1C and 1D). Hierarchical or k-means methods produced nearly identical clusters (>96% of voxels were the same for each cluster). This analysis revealed three statistically significant clusters that differed in their predominant sources of input: (1) posterior-dorsal LP (pLP; cluster 1) receives input primarily from SCs and ventral stream visual cortical areas (laterointermediate area [LI] and postrhinal area [POR]); (2) anterior-ventral LP (aLP; cluster 2) receives input primarily from V1 and dorsal stream visual cortical areas (anterolateral area [AL], rostrolateral area [RL], anteromedial area [AM], and posteromedial area [PM]); and (3) medial LP (mLP; cluster 3) receives input from frontal cortical areas. Importantly, projections from any given source area were biased toward but not exclusive to one of these three clusters; the clusters are therefore defined by dissimilar but overlapping patterns of input (Figure 1C).

Similar patterns of axonal labeling were observed in LP when we limited our analysis to smaller visual cortical injections guided by intrinsic signal imaging or when fluorophore expression was restricted to synaptic terminals (rather than fibers of passage) or to layer 5 or 6 cortical neurons (in Rbp4-KL100 or Nstr1-GN220 Cre mice, respectively; Figures S1C-S1J). Input from layer 5 and 6 neurons from a given area overlapped more with each other than layer 5 and 6 input from separate areas (Figure S1K).

LP Output Mapping Reveals Reciprocal and Relay Transthalamic Pathways

What are the projection targets of these LP subregions? We defined LP output volumes by measuring fluorescence from LP cells retrogradely labeled by rabies injections into 10 target regions, including the amygdala and nine of the cortical areas from the input analysis (Figure 2A; Figures S2A-S2F). These output volumes were mapped to the CCF for comparison with input volumes.

To quantify LP input-output connectivity, we compared the overlap of anterogradely labeled axons and retrogradely labeled cell bodies from each input source and output target (Figure 2B). This analysis revealed putative transthalamic pathways linking visual areas by indirect projections through LP. We found that most of these pathways are reciprocal: if an LP voxel receives input from a region, then it tends to project back to that region (as evident from high values along the diagonal in Figure 2B). However, we also found evidence for relay pathways linking distinct areas (as evident from values off the diagonal). For example, mLP voxels (cluster 3) receive input almost exclusively from frontal cortical regions (ACA and ORB) and project back to these regions as well as to dorsal stream visual cortical areas (PM, AM, RL, and AL). Similarly, aLP voxels (cluster 2) receive most of their input from dorsal stream visual cortical areas but project both back to these regions and to ventral stream visual cortical areas (LI and POR). Finally, pLP voxels (cluster 1) project to the amygdala (LA) in addition to strong reciprocal connections with LI and POR and sparse projections to dorsal stream areas (in particular AL and RL).

A complementary analysis using maps of LP output defined by anterograde tracer injections in different portions of LP yielded similar results (Figures S2G-S2I). This analysis also revealed which layers LP axons target in each cortical area. We found that injections into anterior and posterior LP produced similar patterns of axons in their respective cortical targets (Figure S2J). Interestingly, however, the layer distribution of LP axons differed across cortical areas. To explain this variability, we ordered areas by their position in the cortical hierarchy according to a recently published metric (Harris et al., 2018). We found that areas lower in the cortical hierarchy received a larger proportion of LP axons in layer 1, whereas areas higher in the hierarchy received a larger proportion input in layer 4 (Figure S2K).

Cortical areas are connected directly through cortico-cortical projections and indirectly through higher-order thalamic regions such as LP (transthalamic pathways). To determine whether the same or different visual cortical areas are connected via cortico-cortical and transthalamic pathways (Figure 2C, inset), we compared (1) the density of axons from each cortical area to all other cortical areas (cortico-cortical projections; Figure 2D) with (2) the overlap of axons in the LP from each cortical area (input volumes) and the cell bodies in the LP (output volumes) projecting to each of those areas (transthalamic connections; Figure 2B). There is a significant correlation between these measures of cortical connectivity (Figure 2C), suggesting that transthalamic connections of visual cortical areas through LP largely mirror direct cortico-cortical pathways. Additionally, the greater overlap evident in the transthalamic connectivity matrix indicates that LP may also supplement direct cortico-cortical connectivity by providing additional routes of communication between cortical areas.

Finally, LP is known to project to the dorsal striatum; however, little is known about the topography of this projection. Analysis of injections into the LP from the Allen Connectivity Database revealed a coarse topography of LP output to the dorsal striatum, with more posterior regions of LP targeting the posterior-lateral striatum and more anterior regions in LP targeting the anterior-medial striatum (Figure S2L).

Ventral Stream Areas Participate in Cortico-Collicular-Thalamic Loops

All visual cortical areas in mice project to SCs as well as to deeper SC layers (SCd). Cortical projections exhibit stream-specific biases to SCs (ventral stream areas) or SCd (dorsal stream areas) (Wang and Burkhalter, 2013) and may provide a route by which some visual cortical areas can indirectly influence their input from LP (Figure 2E, inset). To identify potential loops connecting LP, cortex, and SC, we compared (1) the relative strength of input from each cortical area to SCs and SCd with (2) the overlap of SCs input to LP with each cortical area's input to or output from LP (the top rows in Figures 1B and 2B, respectively). We found that the ventral stream areas (LI and POR) that project strongly to SCs are also strongly interconnected with the SCs-recipient portion of LP (Figures 2E and 2F). In contrast, dorsal stream and frontal areas that project strongly to SCd are less connected with the SCs-recipient portion of LP. The geniculo-recipient cortical areas (V1 and lateromedial area [LM]) project strongly to SCs like ventral stream areas but, similar to dorsal stream areas, are relatively weakly connected with SCs recipient LP. Thus, ventral stream areas are the main cortical component of a trisynaptic loop connecting pLP, cortex, and SCs (Figure 2G).

Conversely, we find evidence for only a weak projection to LP from SCd. Allen Connectivity Database injections that more strongly overlapped SCd than SCs labeled relatively sparse axons in pLP (probably because of the small amount of virus in SCs) and mLP (Figure S1L), suggesting that the SCd projects to mLP and that aLP does not receive input from the SCs or SCd. However, the SCd projection to mLP is much sparser than the SCs projection to pLP.

The LP Contains at Least Two Maps of Visual Space Corresponding to SC-Recipient and V1-Recipient Subregions

If the LP subregions we defined anatomically are functionally distinct, then they may, like visual cortical areas, have separate maps of visual space. Indeed, SC and V1 contain full representations of visual space but project to largely nonoverlapping parts of LP (Figures 1A and 1B). We used the retinotopic organization of SC and V1 and the topography of their axons in LP to predict the representation of visual elevation and azimuth in LP (Figures 3A-3F and S3). The predicted elevation map showed separate spatial gradients of visual elevation representation in LP that converge at the boundary of SC and V1 input to LP. Thus, anatomical connectivity predicts that LP contains at least two distinct representations of visual elevation.

To test this prediction, we used Neuropixels high-density electrode probes (Jun et al., 2017) and a sparse noise stimulus to measure the spatial receptive field location of neurons over the full extent of LP in awake mice (Figure 3G). The location of each probe in LP was

marked with DiI, and every recorded cell was assigned a position in the CCF (Figures 3H and 3I; 1,579 neurons; STAR Methods). The dispersion of receptive field locations of nearby neurons was substantially higher in LP than in the dorsal lateral geniculate nucleus (dLGN; Figure 3J). Nonetheless, averaging the receptive field locations of nearby LP neurons revealed a smooth map of elevation that, like the elevation map predicted by anatomy, reversed its gradient near the center of LP, where SC and V1 axons converge (Figure 3K). We confirmed our findings from the population data by serially recording responses to sparse noise in multiple locations across LP in the same mouse (Figure 3L). As we moved the probe to more anterior locations, the receptive field elevation gradient reversed (Figure 3M). These data strongly suggest that pLP and aLP are functionally distinct subregions containing separate maps of visual space. Neurons in mLP were distinct in that they rarely responded to the sparse noise stimulus (Table 1), consistent with the fact that their main input originates in frontal and not visual cortex.

Similar methods were used to construct maps of azimuth representation in LP. Both the topography of axons and the measured receptive fields showed a gradient of azimuth representation in the region of LP receiving input from V1 but no clear azimuth map in the region of LP receiving SC input (Figure S3).

We found evidence for three LP subregions with distinct representations of visual space. Which rules govern the representation of each visual cortical area within these subregions? Visual cortical areas in mice often contain incomplete retinotopic maps biased to a particular region of visual space (Garrett et al., 2014; Zhuang et al., 2017). These biases might be reflected in the organization of cortical connections with LP. We computed the elevation bias for the portion of LP receiving input from, or projecting to, each cortical area by weighting the LP elevation map by the anatomical input and output volumes shown in Figures 1 and 2. We found a significant correlation between these elevations and the mean elevation measured for each cortical area via intrinsic imaging (Figures S3Q-S3T). This result indicates that the LP input and output maps associated with a given visual cortical area are in part predicted by that area’s retinotopic bias.

Mapping receptive field organization in pLP is potentially complicated by the fact that this region contains adjacent zones receiving unilateral or bilateral SC input (Zhou et al., 2017). In other species, SC axons are topographically organized in the part of the LP receiving unilateral input but more diffuse in the part receiving bilateral input (Baldwin et al., 2011, 2013; Chomsung et al., 2008). We found that SC axons are topographically organized for elevation but not azimuth in both the unilateral and bilateral SC-recipient portions of LP (Figure S4), consistent with data from rats (Takahashi, 1985). However, this organization was more precise in unilateral SC-recipient LP (Figure S4H).

Mapping Functional Properties across LP with High-Density Electrophysiology

By registering our LP recordings to the CCF, we were able to map visual response properties across LP and compare these functional maps to the anatomically defined subregions we describe above. We compared visual responses in pLP (the subregion that receives dense input from SC), mLP (the subregion that receives dense input from the ACA), and aLP (sparse, if any, input from the SC or ACA). In addition, we compared visual responses

in LP to putative LP-projecting SC neurons recorded in Nstr1-GN209 Cre x Ai32 mice. In these mice, the SC cell type that projects to LP, but not other SC cell types, expresses channelrhodopsin-2 (ChR2) and responds with sustained spiking to long flashes of blue light (Gale and Murphy, 2016). There are minimal, if any, connections between these LP-projecting cells and other SC cell types (Gale and Murphy, 2018). Consistent with previous results, the visual responses of optotagged SC neurons differed substantially from those of non-optotagged SC neurons recorded in the same mice (Figure S5). By characterizing the visual response properties of neurons in the three LP subregions and identified LP-projecting SC neurons, we are able not only to map functional differences across LP but also to elucidate how visual information in SC is transformed in LP before it is conveyed to the visual cortex.

Receptive Field Size and Size Tuning Differ across LP Subregions

Reponses to sparse noise consisting of black and white squares of varying sizes revealed subregion-specific differences in the size and shape of spatial receptive fields and size tuning in LP. Receptive fields in pLP were horizontally elongated and significantly larger than aLP and mLP receptive fields (Figures 3N and 3O; Table S2; median aspect ratio: 1.30 pLP, 1.15 aLP, 1.05 mLP, and 1.07 SC). Despite their large spatial receptive fields, pLP neurons, like optotagged SC neurons, responded most strongly, on average, to the smallest square size presented (5°; Figures 3N and 3P). These neurons thus respond best to small stimuli presented at any location within a relatively large region of space. In contrast, aLP and mLP neurons responded most strongly to the largest square size (20°). These results are consistent with functional differences, in addition to anatomical differences, between LP subregions.

Responses to Object and Background Motion Differ in LP Subregions

LP-projecting cells in SC respond more strongly to small, slowly moving objects in the visual field than to full-field background motion (Gale and Murphy, 2016). To determine whether LP neurons respond differentially to object or global motion, we recorded responses to a stimulus consisting of a moving random checkerboard background (full field) and a small (10°), differentially moving “patch” of a random checkerboard pattern. Because the patch is only visible when its speed and/or direction of motion differs from that of the background, this stimulus is well-suited to probing responses to object versus global motion (Frost et al., 1988). Responses to a matrix of 7 patch and 7 background velocities were recorded (Figures 4A-4D). To visualize and compare responses across cells, we compiled an N cells (1,135) by 49 conditions (patch and background velocity combinations) population response matrix (Figure 4E). Hierarchical clustering on this matrix revealed three main clusters among which cells from SC and the three LP subregions were differentially distributed (Figure 4E, right).

LP-projecting SC neurons almost exclusively belonged to a cluster of cells that responded most strongly to the patch moving over a stationary background (top cluster with relatively high values in the middle columns of Figure 4E). In some cases, these neurons also responded moderately when the patch and background moved in opposite directions and/or with a large difference in speed. Neurons in pLP were similar to SC but more likely to be modulated by background motion and were split between the patch-selective cluster

(top) and the middle cluster, in which many cells exhibited preferences for the direction and/or speed of patch and background motion. By contrast, cells in aLP and mLP almost exclusively belonged to this middle cluster or the bottom cluster, in which cells were visually responsive but not selective.

Responses to patch versus background motion were summarized by two metrics: (1) plotting response size as a function of background motion (Figure 4F) and (2) calculating a "patch-background index" comparing maximum responses with patch or background motion alone (Figure 4G). Consistent with the clustering shown in Figure 4E, SC and pLP neurons, on average, responded maximally when the patch moved over a stationary background (background speed, 0°/s; Figure 4F) and, unlike aLP and mLP neurons, exhibited a strong bias for positive patch-background index values (indicating a preference for patch motion; Figure 4G; Table S2). Overall, these data further imply that pLP is functionally distinct from aLP and mLP and, along with size tuning data (Figures 3N and 3P), are consistent with the possibility that input from SC plays an important role in shaping visual responses of pLP neurons.

Responses to full-field drifting gratings revealed additional differences in motion sensitivity between neurons in LP subregions. Neurons in aLP and mLP typically preferred faster speeds and higher temporal frequencies than pLP neurons (Figure S6). Direction-selective neurons in pLP tended to prefer motion toward the upper temporal visual field, similar to the bias found in SC (Ahmadlou and Heimel, 2015; Dräger and Hubel, 1975; Gale and Murphy, 2014; Figure S6G), whereas neurons in aLP and mLP tended to prefer motion toward the nasal visual field (Figures S6H-S6J).

Posterior LP Neurons Respond More Strongly to Looming Stimuli

The portion of LP that receives input from SC and projects to the amygdala has been implicated in mediating a freezing response to looming stimuli (Shang et al., 2018; Wei et al., 2015). To characterize responses of LP neurons to looming stimuli, we presented expanding spots that increased in angular size at a rate that simulates an object approaching at constant speed; the rate of expansion is a nonlinear function of time to collision and the object's size/speed ratio (Gabbiani et al., 1999; Figure 5A). SC and pLP neurons responded more strongly to looming stimuli than aLP or mLP neurons (Figure 5C; Figure S8A). Most cells that responded to looming stimuli also responded to the checkerboard stimulus (23 of 23 SC, 110 of 113 pLP, 11 of 13 aLP, and 22 of 26 mLP). In many SC and pLP neurons, the time of the peak response to looming stimuli was linearly related to the object size/speed ratio so that the peak response occurred at a constant angular spot size (Figure 5B). Similar responses to looming stimuli are observed in other animals and are referred to as η cell responses (de Vries and Clandinin, 2012; Gabbiani et al., 1999; Liu et al., 2011; Sun and Frost, 1998). Other types of responses (e.g., ρ and τ cells) were not clearly observed in our experiments (Figure S6L). We define η cells as those with correlations greater than 0.9 between the time of peak response and the object size/speed ratio. Cells defined as η cells were more common in pLP than in other parts of LP (64% of LP-projecting SC, 25% of pLP, and 5% of aLP and mLP neurons; Figures 5D and 5E). Within pLP, other properties of η cells also differed from non-η cells. In response to the checkerboard stimulus, pLP η cells

exhibited a stronger preference for object (patch) motion compared with background motion than non-η cells (Figure 5F). Thus, a population of pLP neurons may convey information about looming stimuli, and object motion in general, to the amygdala and ventral stream visual cortical areas.

Clustering LP Neurons Based on Visual Response Properties Alone Independently Segregates Posterior and Anterior Neurons

Our results demonstrate that different patterns of anatomical connections segregate LP into subregions that contain neurons with different functional properties. Is the inverse also true? Do functional properties predict the spatial organization of neurons in LP? Hierarchical clustering of LP neurons based on visual response properties (size tuning, receptive field [RF] area, and patch-background index) produced two statistically significant clusters (Figure 6A). Compared with neurons in cluster 1, neurons in cluster 2 had larger receptive fields, stronger surround suppression, and a stronger preference for object motion compared with background motion (Figures 6C-6E). These properties are similar to those of neurons located in pLP. Indeed, 52% of pLP neurons were assigned to cluster 2, whereas only 7% of aLP neurons and 3% of mLP neurons belonged to this cluster (Figure 6B). Thus, functional properties independently predict spatial segregation of neurons in LP.

Modulation of LP Neurons by Motor Activity

A subset of LP neurons that project to V1 are modulated by motor activity, running and eye movements in particular (Roth et al., 2016), in addition to visual stimuli. To test whether neurons across the three LP subregions were modulated by running, we compared visual responses to checkerboard and grating stimuli during trials when mice were stationary or running (Figures S7A-S7D). We found a weak but significant facilitation of visual responses during running in all LP subregions, with pLP being the least modulated. Cells that were modulated during the checkerboard stimulus tended to be similarly modulated during drifting gratings (Figure S7D).

We also tested whether LP neurons were sensitive to eye movements by recording neural activity and eye position in the dark. Aligning the activity of LP neurons to the initiation of horizontal saccades revealed cells that were either excited or suppressed by eye movements (Figures S7E-S7N). The fraction of cells that were significantly modulated during saccades was similar across LP subregions (22%–24% excited, 6%–10% inhibited; n = 363 pLP, 472 aLP, and 49 mLP neurons from mice in which we recorded at least 10 saccades in the dark). In SC, 2 of 11 optotagged cells were excited and none were inhibited during saccades.

V1 and SC Input Drive Visual Activity in Separate LP Subregions

Our results show that the visual response properties of pLP neurons are similar in several characteristics to those of SC neurons that project to pLP. However, it is unclear whether input from SC alone drives visual responses in pLP. In theory, the retino-geniculate-V1 pathway could provide the primary drive to pLP through both the sparse direct projection from V1 to pLP and indirect connections through higher visual areas (Figure 2G). Direct retinal input to LP could also contribute to pLP activity, although this input is sparse and primarily from non-image-forming melanopsin-expressing retinal ganglion cells (Allen et

al., 2016). Conversely, although SC does not project directly to aLP, it could influence aLP through indirect pathways. To determine the relative effect of cortical and SC input to LP, we recorded spontaneous activity and visual responses of LP neurons while suppressing activity in the visual cortex or SC.

To suppress activity in the visual cortex, we directed blue light over V1 in VGAT-ChR2 mice (Figure 7A; this manipulation activates inhibitory neurons, which potently suppresses the local cortical network; Zhao et al., 2011). Cortical suppression strongly reduced both spontaneous activity and responses to the checkerboard stimulus in aLP neurons (Figures 7B-7F). To a lesser extent, spontaneous activity and visual responses were also reduced in pLP neurons (Figures 7C, 7D, 7G, and 7H). Unlike aLP neurons, the strength of suppression of visual responses in pLP neurons depended on the stimulus condition ($p = 0.019$ for pLP, $p = 0.83$ for aLP, Kruskal-Wallis test). In pLP neurons, responses to the checkerboard patch moving over a stationary background were weakly suppressed compared with responses when the background was moving (Figure 7H). Consequently, when the cortex was inactivated, pLP neurons more strongly preferred object motion compared with background motion, becoming even more like SC neurons that project to pLP.

The effect of cortical suppression on activity of pLP neurons could partially reflect reduced cortical input to SC neurons that project to the pLP (Zhao et al., 2014; Figure 7A). Thus, we also measured the effect of cortical suppression on SC neurons (note that use of VGAT-ChR2 mice precluded optotagging of LP-projecting SC cells). Cortical suppression moderately reduced visual responses of neurons in the optic fiber layer of SC (SCop), where the somata of LP-projecting neurons are located (Figure S8). Although the suppression of SCop neurons was similar in magnitude to the effect on pLP neurons, it did not significantly depend on checkerboard background speed ($p = 0.86$, Kruskal-Wallis test). Thus, suppression of SC activity does not fully explain the effects of cortical inactivation on pLP neurons, suggesting that the activity of pLP neurons is most likely shaped by combinations of input from both the SC and cortex.

To directly assay the contribution of the SC to LP visual responses, we inactivated the SC with tetrodotoxin (TTX) while recording in LP. The relative effects of SC inactivation on aLP and pLP neurons were the opposite of those observed during cortical inactivation (Figures 7K, 7Q, and 7R). Spontaneous activity and visual responses were more strongly suppressed in pLP than in aLP (Figures 7K and 7L). Moreover, pLP neurons lost their preference for object motion; responses to the checkerboard patch moving over a stationary background were more strongly suppressed than responses when the background was moving (Figures 7M-7S; $p = 3.7e{-}9$ for pLP, $p = 0.65$ for aLP, Kruskal-Wallis test). Thus, the functional properties of pLP neurons depend critically on receptive field-defining input from SC.

Silencing the visual cortex or SC did not affect the running modulation of visual responses in aLP or pLP (SC silencing—ΔRMI pLP: -0.05 ± 0.3, $p = 0.16$; aLP: -0.02 ± 0.2, $p = 0.16$; V1 silencing—ΔRMI pLP: -0.006 ± 0.2, $p = 0.95$; aLP: -0.002 ± 0.3, $p = 0.36$; where ΔRMI is control – perturbation, Wilcoxon signed-rank test), suggesting that the small

increase in responsiveness during running we observed across LP may reflect ascending neuromodulatory input.

pLP contains subdomains receiving bilateral or unilateral SC input (Figure S4). Because we did not attempt to inactivate the SC contralateral to the LP recording, the effect of silencing the ipsilateral SC might be stronger in the unilateral recipient zone than in the bilateral recipient zone. However, this was not the case because the observed effect was moderately stronger in the bilateral recipient zone (the median checkerboard TTX-MI was −0.30 for cells in the bilateral zone [n = 132] and −0.19 for cells in the unilateral zone [n = 111], p = 0.0032).

Responses to the checkerboard and looming stimuli as well as functional clustering revealed diversity among pLP neurons (Figures 4E, 5F, and 6B), suggesting that some pLP neurons may depend more strongly than others on SC input. Consistent with this possibility, pLP neurons that were most suppressed by SC inactivation showed a greater preference for object motion during control trials than less suppressed pLP neurons (Figure 7T). Thus, functional diversity in pLP is at least in part explained by strength of input from SC.

DISCUSSION

We combined comprehensive anatomical circuit tracing with activity mapping across the entire LP complex in mice. By registering data from multiple modalities to a common anatomical coordinate system, we made quantitative comparisons between anatomy and functional properties. Moreover, silencing the two main LP input pathways showed divergent effects across LP. Neurons in pLP are driven by SC input and respond to looming stimuli and small moving objects. Conversely, neurons in aLP are driven by visual cortical input and respond to large stimuli and full-field motion. A third subregion, mLP, may provide a transthalamic route for information flow from the frontal and associational cortex to visual cortical regions.

Input-Output Connectivity Defines Functionally Relevant Thalamic Subregions

The close correspondence between anatomically and functionally defined LP subregions supports the emerging view that the fundamental units of corticothalamic computation are not individual thalamic nuclei but more precise thalamic circuits linking functionally related cortical areas (Halassa and Kastner, 2017; Shipp, 2003). A potential criticism is that the three LP subregions we define are not truly distinct but lie along a continuum of many input-output microcircuits. However, the reversal of the elevation map and its close correspondence to the merging of axons from SC and V1 suggest that pLP and aLP are functionally distinct zones. Moreover, mLP is defined largely by a unique projection from the frontal cortex that categorically separates it from the other LP subregions. Thus, we believe that our parcellation captures three broad but functionally relevant domains of LP. Nonetheless, it should be noted that both the input and output connectivity between cortex and LP is dense, and most of the connections between these structures that could exist are present, at least to some degree. This dense network topology could allow LP to coordinate activity across different cortical modules. Future fine-grained investigation could reveal more precise microcircuits within each LP subregion.

The rodent LP was previously divided into three subregions—caudomedial (LPcm), lateral (LPl), and rostromedial (LPrm)—based on cytoarchitecture and immunocytochemical markers (Nakamura et al., 2015; Takahashi, 1985; Zhou et al., 2017). These regions differ in several ways from the LP subregions we identified based on anatomical connectivity and functional properties. LPl in previous work likely bridges pLP and aLP in our designation. Moreover, although we include all of the SC-recipient LP in pLP, previous schemes separated LP subdivisions that receive bilateral or unilateral SC input (LPcm and the posterior half of LPl, respectively). In mice, the portion of LP that receives unilateral SC input is relatively small (Figure S4), and individual LP neurons extend their dendrites across the border between LPcm and LPl (Zhou et al., 2017). For these reasons, we did not assign LP units to one or the other SC-recipient subdivision. Future studies may reveal functional differences between pLP neurons that receive bilateral or unilateral SC input.

Transthalamic Pathways Mirror Cortico-Cortical Connections

Our anatomical data suggest that indirect transthalamic pathways connecting cortical areas through LP largely mirror direct cortico-cortical connectivity. This parallel connectivity scheme could enable LP to coordinate cortico-cortical communication by synchronizing activity across cortical areas (Saalmann et al., 2012). How the thalamus modulates or transforms information carried in transthalamic pathways and how these signals differ in content or effect from those of direct cortico-cortical pathways are crucial questions for understanding cortical computation.

The cortical projection to LP originates in both layer 5 (L5) and layer 6 (L6) pyramidal neurons. We found that L5 and L6 neurons from a given cortical area target similar regions in LP (Figure S1K). It has been proposed that L5 provides a strong “driver” input to LP, mediating feedforward transthalamic pathways, whereas L6 acts as a “modulator” in feedback pathways (Sherman, 2016). Our data suggest that both L5 and L6 participate in reciprocal corticothalamic feedback loops, similar to what has been described for frontal cortex connections with the thalamus (Collins et al., 2018). Future studies could reveal unique contributions of L5 and L6 input to transthalamic pathways connecting distinct cortical areas.

Cortical Dorsal and Ventral Streams Extend through Cortico-LP and Cortico-SC-LP Circuits

Network analysis of cortical projections suggests that the mouse visual system can be divided into ventral and dorsal streams similar to those described in other species (Wang et al., 2012). Our analysis of LP input-output connectivity indicates that these cortical pathways are mirrored by cortico-thalamo-cortical projection patterns, with ventral stream areas reciprocally connected with pLP and dorsal stream areas reciprocally connected with aLP. The association of ventral stream areas with SC-recipient LP in mice represents a fundamental difference between the rodent LP and primate pulvinar, in which the SC-recipient inferior pulvinar is most strongly connected with dorsal stream visual areas in the MT complex (Berman and Wurtz, 2010; Lyon et al., 2010). Interestingly, unlike dorsal stream areas in mice, the MT projection to SC is biased toward the superficial layers, similar to SC projections from the mouse ventral stream. Thus, both species feature a loop

connecting LP (or pulvinar), cortex, and SCs despite the fact that the cortical component of that loop resides in the ventral stream in mice and in the dorsal stream in primates. These data provide further evidence that the dorsal and ventral streams in mice are analogous but not identical to the primate visual streams, possibly indicating differences in how these species use vision.

The connectivity of mLP with the frontal and associational cortices resembles the connectivity of the medial and dorsomedial pulvinar in primates (Kaas and Lyon, 2007). Although most mLP neurons were visually responsive, they were less likely to have organized receptive fields, and many did not respond to sparse noise (Table 1). These data suggest that mLP neurons are involved in higher-order visual processing and do not encode simple visual features. In the future, it will be interesting to test whether these cells are particularly sensitive to behavioral context, similar to neurons in the dorsomedial pulvinar (Petersen et al., 1985).

SC Provides Driving, Receptive Field-Defining Input to pLP

Dual retinofugal pathways through LGN and SC are an ancient, highly conserved feature of the vertebrate visual system (Butler, 2008). In primates, the “secondary” visual pathway running through SC and pulvinar has traditionally been thought to play a modulatory role in visual processing, potentially relaying saccade-modulated visual signals (Berman and Wurtz, 2011; Berman et al., 2017). Previous studies disagreed whether SC input could drive receptive field properties in pulvinar neurons (Bender, 1983; Casanova and Molotchnikoff, 1990), perhaps depending on species and/or where in the pulvinar recordings were made. Our data show that pLP neurons are tuned similarly to their input from SC. Moreover, silencing SC dramatically suppresses visual responses of pLP neurons and abolishes their preference for object motion (Figure 7). Together, these results demonstrate a major role for SC in driving visual responses in pLP and establish that the secondary visual pathway is an important parallel stream running alongside the geniculo-cortical pathway, consistent with recent results (Beltramo and Scanziani, 2019). Our data further suggest that this pathway is particularly important for carrying information about looming or small moving objects.

Differences between pLP and pLP-projecting SC neurons suggest that pLP is not a simple relay of SC input. In particular, receptive fields of pLP neurons are substantially larger and horizontally elongated relative to those of LP-projecting SC neurons, suggesting that multiple SC neurons with horizontally displaced receptive fields might converge onto single pLP neurons. Such convergence is consistent with the topographical organization of SC axons for elevation but not azimuth in LP and may explain the lack of an organized map of azimuth representation in pLP.

Cortical and Subcortical Inputs Converge in pLP

Both SC and ventral stream visual cortical areas (POR and LI) project to pLP, suggesting that individual pLP neurons could integrate input from cortical and subcortical sources. Because a large majority of pLP cells were suppressed during both SC and cortical inactivation experiments, many pLP neurons likely combine input from these two sources. Interestingly, SC and cortical inactivation had differential effects on pLP excitability:

cortical inactivation more strongly suppressed spontaneous than visually evoked activity and reduced responses to background motion, whereas SC inactivation more strongly suppressed visually evoked activity and abolished tuning for object motion (Figure 7). Thus, cortical input to pLP may provide tonic modulatory drive as well as information about visual context and object identity, which could be integrated with object motion signals from SC.

The relative strength of cortical and SC input could underlie the functional diversity of pLP neurons. Indeed, we found visual tuning differences between pLP neurons that were strongly or weakly suppressed by SC inactivation (Figure 7T). Moreover, neurons in pLP were split between two functionally defined clusters, only one of which closely resembles SC input (Figure 6). Responses to checkerboard and looming stimuli also revealed functional diversity in pLP (Figures 4E and 5F). The degree to which driving inputs from one or more sources (e.g., SC and/or cortical areas) converge on individual neurons is a critical outstanding question for LP and higher-order thalamic nuclei in general (Groh et al., 2014; Mease et al., 2016).

Recent studies have shown that the higher-order thalamus plays a fundamental role in shaping and maintaining cortical activity (Guo et al., 2017; Purushothaman et al., 2012; Schmitt et al., 2017; Zhou et al., 2016). Our comprehensive characterization of the structural and functional organization of the mouse LP provides a roadmap to decipher circuit-specific mechanisms by which the higher-order thalamus contributes to visual processing and behavior.

STAR★METHODS

CONTACT FOR REAGENT AND RESOURCE SHARING

Further information and requests for resources and reagents should be directed to and will be fulfilled by the Lead Contact, SG (samg@alleninstitute.org).

EXPERIMENTAL MODEL AND SUBJECT DETAILS

Rabies injections in visual cortical areas were performed at the Salk Institute and approved by the Salk Institute's Institutional Animal Care and Use Committee (IACUC). All other experiments were performed at the Allen Institute using methods approved by the Allen Institute's IACUC, with the exception that one pharmacological agent (TTX) was inadvertently omitted from the IACUC protocol, but has subsequently been added and approved for future experiments. Mice of either sex were used and were > 70 days old on the day of electrophysiological recordings. Transgenic mice were maintained on a C57BL/6J background. The number of mice used for each experiment is indicated in Table 1 and Table S1.

METHOD DETAILS

Anatomy—To generate LP input maps (Figure 1A), we utilized publicly available anterograde tracing data from the Allen Mouse Brain Connectivity Database (Oh et al., 2014) (Table S1). For cortical areas, we used injections in C57BL/6J, Emx1 Cre, Rbp4-KL100 Cre, or Ntsr1-GN220 Cre mice. For SC, we used injections in C57BL/6J mice with

viral expression in the superficial layers (experiments 112827164, 114754390, 126646502, 128001349, and 146078721). Experiments with injection volumes less than 0.05 mm^3 were excluded. For injections in visual cortical areas, experiments with injection volumes greater than 0.25 mm^3 were also excluded. For each source of input to LP, we averaged "projection energy" volumes aligned to the Allen Mouse Common Coordinate Framework (CCF; 25 μm^3 voxels) after normalizing by the brightest voxel in LP. Voxels in LP were then smoothed in three dimensions with a Gaussian kernel with standard deviation of 75 μm. Maximum-intensity projections of smoothed LP voxels in the horizontal and sagittal planes are displayed in Figure 1A. For all analyses (e.g., comparing overlap of axons from different sources or clustering) the entire volume of voxels in LP were used.

To generate LP output maps (Figure 2A; Figure S2), we injected G-deleted rabies encoding fluorescent protein into each of the LP targets shown in Figure 1 (SADΔG-EGFP or mCherry derived from the SAD B19 vaccine strain of rabies; Wickersham et al., 2007). For injections in visual cortical areas, injections (35-150 nL, 350 μm deep) were targeted to the center of visual areas identified by intrinsic signal imaging (Garrett et al., 2014). Anterior cingulate (ACA) injections were 0.5 mm anterior and 0.25 mm lateral from bregma and 0.5 mm deep from the pia (100-150 nL). Lateral amygdala (LA) injections were 1.3-1.8 mm posterior and 3.1-3.3 mm lateral from bregma and 3.4-4.2 mm deep from the pia (50 nL at each of three depths). Mice were perfused seven days after rabies injection. Images of 50-100 μm thick coronal sections were aligned to the CCF in three steps. (1) Images were downsampled to 25 μm pixels and the first and last sections were manually aligned to the CCF template brain. Intermediate sections were then aligned via interpolation. (2) A global affine transformation (scale, rotation, shear) was applied to each section. The transformation matrix was obtained by comparing binarized versions of the image and corresponding template section using the Open Source Computer Vision Library function findTransformECC. (3) Local warping was applied using manually defined key points on the image and corresponding template section. Delauney triangles were defined from the key points, and affine transformations were applied to warp each triangle in the image to the location of the corresponding triangle in the template section. CCF-aligned rabies-injected brains were averaged and smoothed as described for anterograde tracing data to generate the images and analysis shown in Figure 2. The extent of LP that projects to V1 is probably underestimated due to the small number of injections targeted to the center of this relatively large visual area.

To verify that the fluorescence we quantify in LP output volumes reflects retrogradely labeled LP cells and not anterogradely labeled processes from other regions, we considered the following: many (if not all) layer 5 visual cortical neurons that project to LP also send axon collaterals to SC. We did not observe labeled axons in SC from rabies injections in cortex (e.g., Figures S2A and S2C). The maximum voxel intensity in SC for all of the cortical rabies injections was only 2.7% ± 1.8% of the maximum voxel intensity in LP, indicating that the signal we measure in LP from rabies injections in cortex does not come from anterogradely labeled cortical axons. Moreover, we counted cell bodies for a subset of our raw image data (one coronal section in pLP and one in aLP/mLP) and found a strong correlation between the cell count and the total fluorescence in LP in the final smoothed volume for corresponding sections (r-squared = 0.76, p = 9.8e-6).

Input or input-output overlap was quantified by computing the normalized dot product of LP voxels in the average, smoothed volumes of anterograde (inputs) or retrograde (outputs) label (Figures 1B and 2B). For each comparison, the dot product of the vectors of LP voxels were divided by the product of the length of these vectors.

To complement LP output volumes defined by retrograde rabies labeling, we analyzed anterograde tracing data from LP injections in the Allen Connectivity Database (Figures S2I-S2K). Injections were excluded if the injection volume was larger than 0.26 mm^3 or smaller than 0.01 mm^3, resulting in 13 injections. For each injection, the projection to each visual area was normalized by the total projection density to all visual areas. Output volumes were then computed for each target region by weighting the LP injection volumes by their normalized projection density to that region and smoothing with a 100 μm standard deviation Gaussian kernel in three dimensions. Due to potential viral labeling of nearby neurons in dLGN, output volumes were not calculated for V1 or lateromedial visual cortex (LM), which are known to receive strong projections from dLGN. We also used this dataset to assess the topography of LP projections to the dorsal striatum (Figure S2N). To make this figure panel, the projection density for each LP injection was thresholded at 20 percent of the maximum voxel in the dorsal striatum (STRd) and colored according to the location of the injection centroid in the posterior-anterior axis. A subset of these LP injections were also used to quantify the laminar pattern of LP input to visual cortex (Figures S2L and S2M). Five of the 13 injections were excluded due to direct labeling in dLGN. For the remaining 8 injections, the projection density to each visual area and layer were compiled into a layer x area matrix. Layer 6b data were found to include white matter axons and was excluded from analysis. To make Figure S2M, these projection matrices were normalized by their peak value and averaged across injections. The columns of the resulting matrix (visual areas) were then ordered according to the visual hierarchy index in Harris et al. (2018) and normalized to sum to 1.

To analyze cortico-cortical connectivity (Figure 2D), we combined injections from the Allen Connectivity Database for each cortical area. Injections were excluded if they were larger than 0.2 mm^3 or smaller than 0.05 mm^3 or resulted in a total density of less than 0.005 mm^3 across all cortical targets. Injections into transgenic lines labeling inhibitory cells or with sparse cortical expression were also excluded. Each remaining injection was normalized by its total projection density across the targets listed in Figure 2D. The strength of the projection from area X to area Y was defined as the median normalized projection density in area Y across all injections into area X. The resulting connectivity matrix was then row normalized to make Figure 2D.

To analyze cortical projections to SC, we used the same injections used to quantify LP input but excluding injections in Ntsr1-GN220 Cre mice (which labels layer 6 cortical neurons that do not project to SC). We computed the difference of the median projection density in SCs and SCd divided by their sum. This quantity (y axis in Figures 2E and 2F) was compared to the overlap between SCs input to LP and either the LP input or output volume for each cortical area (x axis in Figures 2E and 2F, respectively).

To analyze the topography of SC and V1 input to LP (Figures 3 and S3), we primarily used anterograde tracing data from the Allen Connectivity Database. For V1, we used injections in C56BL/6J or Emx1 Cre mice with injection volumes between 0.05 and 0.25 mm^3. To supplement the SC injection dataset (Table S1), we injected AAV-2.1-CAG-Flex-GFP and AAV-2.1-CAG-Flex-tdTomato into the SC of Ntsr1-GN209 Cre mice (Gerfen et al., 2013). In these mice, Cre expression in superficial SC is restricted to cells that project to LP (Gale and Murphy, 2014, 2018). AAV was injected iontophoretically from a pipette with tip diameter of 20 μm using 3 nA current applied 7 s on, 7 s off for 3 min. Both viruses were injected into each mouse, offset along the medial-lateral or anterior-posterior axis (Figure S4J). One of the injections failed in 4 of 8 mice, resulting in 12 injections suitable for analysis. Images from these mice were aligned to the CCF as described for LP output mapping.

For each SC (n = 17) or V1 (n = 33) injection, we calculated injection and projection centroids in CCF coordinates using injection or projection density data (for injections from the Allen Connectivity Database) or raw fluorescence normalized to the brightest pixel in LP (for our SC injections). Injection centroids were defined as the average CCF coordinate of voxels in SC or V1 with density or normalized intensity greater than 0.25, weighted by their density/intensity. Projection centroids were similarly calculated using voxels in LP. V1 injection centroids were assigned elevation and azimuth values based on ISI maps of elevation and azimuth aligned to the CCF and averaged across mice (Figures 3 and S3). SC injection centroids were assigned elevation and azimuth values based on their position along the medial-lateral or anterior-posterior axis, respectively, which approximates the measured receptive field maps of SC neurons (Dräger and Hubel, 1976) and the topography of V1 projection centroids in SC (Figures S3D and S3K). Projection centroids were assigned the same elevation/azimuth as their corresponding injection centroids. To generate smoothed elevation and azimuth maps, projection centroid elevation or azimuth values were smoothed in three dimensions with a Gaussian kernel with standard deviation of 100 μm (SC and V1 data were smoothed separately and then combined in a single volume).

To compare LP input and output volumes to the retinotopic bias of each cortical visual area (Figures S3Q-S3T), we utilized a mean elevation map for visual cortex based on ISI imaging from 14 mice (dataset from Garrett et al., 2014). For each visual area, we assigned a “measured” elevation value corresponding to the mean of the ISI elevation map over that area. We then computed two “predicted” elevations for each area by weighting the LP elevation map by either its anterograde input volume or rabies-based output volume (from Figures 1 and 2).

Injection IDs for all experiments in the Allen Connectivity Atlas used in this paper are available as supplemental material (Table S3).

Electrophysiological recordings—Electrophysiological recordings from SC, LP, dLGN, or V1 neurons were made with Phase 2 Neuropixels probes (Jun et al., 2017) (128 channels arranged in two columns, with 20 μm between each recording site). Data were acquired at 30 kHz using the Open Ephys acquisition board and GUI (Siegle et al., 2017) and high-pass filtered (300 Hz). Mice were habituated to the recording rig for at least two

weeks. On the rig, mice were head-fixed and allowed to run on a styrofoam cylinder covered with rubber matting. On the day of recording, mice were anesthetized with isoflurane and a small craniotomy was made above the target brain region in the left hemisphere and covered with Qwikcast (World Precision Instruments). Mice recovered for at least 2 h before recordings. For most mice, this procedure was repeated the following day for a new recording location (Table 1).

Optotagging SC neurons—The SC cell type that projects to LP was identified ("optotagged") by channelrhodopsin-2 (ChR2) activation in Ntsr1-GN209 Cre x Ai32 mice (Gerfen et al., 2013; Madisen et al., 2012). Previous studies have shown that in these mice, ChR2 expression in SCs is limited to the cell type that projects to LP (Gale and Murphy, 2016). Given that these cells display little if any connectivity with other SCs cell types (Gale and Murphy, 2018), cell identification in these mice is not complicated by local recurrent connectivity. During these recordings, a 50 μm core diameter optical fiber was inserted in the brain near the Neuropixels probe to a depth just above the SC (~1 mm). Blue light was used to activate ChR2-expressing cells (2 s pulses, 0.5-10 mW measured from the fiber tip). Cells were considered optotagged if their mean firing rate during the last 1 s of the light pulses was greater than 5 standard deviations above the mean spontaneous rate. Spontaneous rate was calculated from the 1 s bin preceding each light pulse. The functional properties of optotagged cells in this study largely resemble those using the same method in a previous study (Gale and Murphy, 2016), though we find that they have slightly smaller receptive fields. Possible reasons for this difference include anesthesia used by Gale and Murphy (2016) and the different visual stimulus and analysis methods used to define receptive field area.

Visual Stimuli—The mouse's head was fixed at the center of a 24-inch diameter spherical dome (Figure 3G). Visual stimuli were projected on the inner dome surface from two laser projectors (one on each side of the mouse) pointed at spherical mirrors placed below the running wheel. Four different visual stimuli were presented. (1) Sparse noise consisted of dark (0.6 cd/m^2) and light (5.8 cd/m^2) squares (5, 10, or 20° across) presented one at a time for 100 ms on a gray background (3.2 cd/m^2). The stimulus center position for each trial was chosen pseudo-randomly from a grid of 10° spacing and ranging from −20 to 120° in azimuth (negative is left of straight in front of the mouse) and −30 to 90° in elevation (negative is below the eye). Full-field flashes were also presented. All of the stimulus positions, sizes, and contrasts were sampled once per loop in random order before initiating a new loop. (2) Two sets of moving gratings stimuli were presented. For both, the gratings filled the entire right side of the dome, drifted for 2 s, and were followed by a 1 s gray screen period before the next trial. The first set of gratings included two orientations (vertical gratings moving in the nasal-to-temporal direction and horizontal gratings moving downward), six spatial frequencies (0.01, 0.02, 0.04, 0.08, 0.16, and 0.32 cycles/^{0}) and five temporal frequencies (0.5, 1, 2, 4, and 8 cycles/s), for a total of 60 trial types. Each trial type was presented once in random order before beginning a new loop. The second set of gratings included eight directions of motion, two spatial frequencies (0.02 and 0.16 cycles/^{0}), and two temporal frequencies (1 and 4 cycles/s). (3) A checkerboard stimulus consisted of random patterns of dark and light 1° squares that filled both sides of the dome.

The background checkerboard pattern moved such that the right and left halves converged (temporal-to-nasal motion) or diverged (nasal-to-temporal motion) at the point directly in front of the mouse. Simultaneously, a 10° patch, also consisting of a random pattern of dark and light 1° squares, moved horizontally with direction and speed independent of that of the background checkerboard pattern. Patch and background velocities were −90, −30, −10, 0, 10, 30, and 90 ^{0}/s (positive velocities are the nasal-to-temporal direction). The patch is invisible when the patch and background velocities are the same. The patch was presented at 0 and 40° elevation for LP recordings or targeted to the multi-unit receptive field elevation for SC recordings. (4) Looming stimuli were light or dark spots that expanded to simulate an object approaching at constant speed (Gabbiani et al., 1999). The expansion rate is a nonlinear function of time-to-collision and the object's size/speed ratio, which was 10, 20, 40, or 80 ms. The initial spot radius was 0.5° and the final spot radius was 80°, which was held for 0.5 s before a 2 s gray screen inter-trial interval.

Cortical inactivation—Cortical inactivation experiments were conducted in VGAT-ChR2 transgenic mice (Zhao et al., 2011). Before each experiment, two optical fibers (200 μm core diameter) were positioned over the skull over left V1 by stereotaxic coordinates (relative to lambda, the two fibers were 0 and 1 mm anterior and 2.8 and 2.6 mm lateral). Each fiber was coupled to a blue laser or LED calibrated to produce 2.5 mW measured at the fiber tip. During the sparse noise stimulus, control and cortical silencing conditions were interleaved in 25 trial (2.5 s) blocks. For all other stimulus protocols, control and cortical silencing trials were interleaved. Light delivery began one second before each silencing trial and ended 100 ms after the trial. Power was linearly ramped (100 ms) on and off. To allow cortex to recover after cortical silencing, four seconds were added between silencing and control trials/blocks. For all perturbation experiments, checkerboard stimulus conditions were reduced (patch and background velocities: −80, −20, 0, 20, 80 ^{0}/s) to increase trial repetitions. In separate mice not used for SC or LP recordings, we measured the lateral spread of cortical silencing using one fiber at 2.5 mW. Consistent with other studies (Guo et al., 2014), we found significant silencing at 1 mm and near complete silencing at 0.5 mm lateral from the fiber tip.

SC inactivation—For SC inactivation experiments, we positioned a glass pipette (15-20 μm tip diameter) filled with 25 μM tetrodotoxin (TTX) into the left SC (0.5-0.7 lateral and 0-0.2 anterior from lambda and 1.2-1.5 deep from brain surface). During pipette insertion, black-white alternating flashes were played in the right hemifield and the visually-evoked potential (VEP) was monitored on an oscilloscope. The VEP became noticeably larger and more consistent at ~1 mm depth, consistent with entry into the SC. The control dataset was collected after pipette insertion but before TTX injection. TTX was then injected by a picospritzer (2-10 PSI). During injection, the TTX pipette meniscus was video monitored to verify an injection volume of ~50 nL. We allowed 5 min after injection for TTX to diffuse before collecting the TTX dataset. The checkerboard stimulus was ongoing throughout the control, injection, diffusion, and TTX epochs. At the end of most experiments we moved the Neuropixels probe from LP to SC to verify the SC silencing. No spontaneous or visual-driven spikes were observed at locations 500 μm from the injection pipette tip. Activity appeared normal 1 mm from the injection pipette tip. Evan's blue (0.005%) was included in the pipette solution, and injection location was verified by post hoc histology.

Eye Tracking—Images of the right eye were acquired at 60 Hz in the dark with an infrared (IR) camera. IR LEDs were placed around the camera lens. The pupil is large in the dark and its edges are partially occluded. Rather than tracking the pupil center, we determined the horizontal position of the lateral edge of the pupil relative to a corneal reflection. Saccade times were detected automatically using a velocity threshold and manually verified.

QUANTIFICATION AND STATISTICAL ANALYSIS

Spike sorting was done in a two-step process. First, spikes were automatically detected and clustered using Kilosort (Pachitariu et al., 2016). Kilosort output clusters were then manually curated in phy (Rossant et al., 2016). All units passing this manual step were included for further analysis.

To register units to the CCF, brains were fixed overnight after the last experimental day and sliced on a vibratome (100 μm coronal sections). The first (posterior) and last (anterior) slices containing LP were aligned to corresponding CCF sections, and the remaining slices were aligned by linear interpolation. The probe track was then registered to the CCF by manually annotating the probe tip and the point at which it entered LP (based on DiI labeling). Individual units were then assigned positions along this track according to the distance from the tip to the channel with the maximum waveform amplitude. A similar method was used for SC recordings. Units were considered to be in LP if they fell within 100 μm of the LP border after CCF alignment (with the exception of dLGN units, which were readily identified by the sharp boundary between dLGN and LP in histological slices).

For analysis of responses to sparse noise, checkerboard, and looming stimuli, a mean spike density function (SDF) was computed for each stimulus condition by convolving the raw spike train with a Gaussian kernel (10 ms standard deviation for sparse noise or 100 ms for checkerboard and loom) and averaging across trials. The response to a given stimulus condition was taken as the peak of the mean SDF over the stimulus window (50-150 ms after stimulus onset for sparse noise, 250 ms to end of trial for checkerboard, or trial onset to collision time for loom). To quantify a cell’s responsiveness to a given stimulus, its peak response was compared to spontaneous activity. A cell was included in the analysis for a given protocol if its peak response across all conditions was greater than 5 standard deviations above the mean spontaneous firing rate. For sparse noise, the spontaneous firing rate distribution was estimated by randomly selecting n trials (where n was the number of repeats of the full stimulus set) and calculating the peak of the mean SDF from stimulus onset to 50 ms (a window that excludes the visual response). This process was repeated 200 times and the resulting 200 mean SDF peaks were taken as the spontaneous firing rate distribution. This same process was used for loom (with 100 repetitions), but the subsampled trials were restricted to those with a size to speed ratio of 80 ms (the longest trials), and the analyzed window ranged from stimulus onset to 1 s after onset. For checkerboard, the spontaneous rate was computed from trials in which the patch and background speed were 0°/s (a static random checkerboard stimulus; the middle square of the checkerboard response matrix).

For gratings stimuli, the response to a given trial condition was defined as the mean number of spikes elicited during that condition in the window from 250 ms after stimulus onset to

stimulus offset. The spontaneous rate was taken from randomly interspersed trials for which the gratings stimulus was omitted (isoluminant gray screen).

To define receptive field location and area, responses to sparse noise as a function of spatial position were smoothed with a two-dimensional Gaussian filter (standard deviation 10°) and then fit to a two-dimensional Gaussian. Cells that did not respond to sparse noise (as defined above) or for which the fitting algorithm failed were not used for receptive field analysis. Receptive area is pi times the product of the major and minor radii of the fit at one standard deviation. To generate the measured LP elevation map, CCF voxels were assigned an elevation based on the mean elevation for cells assigned to that voxel (for the vast majority of voxels this was one or zero units). The resulting map was then smoothed with a Gaussian kernel (standard deviation 100 μm), linearly interpolating values for voxels without data. The same procedure was used for azimuth.

We used two measures to quantify the topographic organization of projection centroids or receptive field locations in LP. The first was the r^2 value of a three-dimensional linear fit of the elevation or azimuth assigned to the CCF coordinate of each projection centroid or receptive field. The second was Moran's I, a measure of spatial autocorrelation, for these same values (Moran, 1950). Randomly dispersed elevations or azimuths result in Moran's I near zero, perfect dispersion (i.e., a "checkerboard" of high and low values) results in a Moran's I near −1, and segregated azimuths or elevations (i.e., high values in one portion of LP and low values in another) results in a positive Moran's I. Standard error of the linear fit r^2 and Moran's I were calculated by randomly sampling (10000 repetitions with replacement) the data and taking the standard deviation of the 10000 resulting values.

To quantify the modulation of visual responses by motor activity in LP, we classified trials as running (mean speed > 5 cm/s) or stationary (mean speed < 1 cm/s). Because animals often spent the majority of the time in one behavioral state (usually running), we matched trial number and stimulus condition by randomly subsampling trials from the behavioral state with more trials. Cells were only included in the running analysis (Figure S7) if they were deemed to have a significant response to the visual stimulus before separating trials by motor activity. The running modulation index was defined as (run + stationary)/(run − stationary), where run and stationary refer to the mean visual response across all stimulus conditions during running and stationary epochs respectively.

To quantify the effects of silencing cortex or SC on LP visual responses, we defined optogenetic and TTX modulation indices (OMI and TTX-MI) as (perturbation−control)/(perturbation+control), where "perturbation" and "control" were the peak visual response for the checkerboard stimulus averaged over the perturbation and control trials respectively. For spontaneous activity, the central square of the checkboard response matrix was used (static background stimulus). Suppression tuning curves were calculated for the best response at each background speed (maxima along the columns of the checkerboard response matrix). Only cells with significant responses to the checkerboard stimulus during control trials were analyzed.

All statistical comparisons were non-parametric, two-sided tests. For all comparisons, the test and p value are given in the Results, figure and legend, or Table S2.

Supplementary Material

Refer to Web version on PubMed Central for supplementary material.

ACKNOWLEDGMENTS

We thank Dan Denman and Josh Siegle for advice regarding Neuropixels recordings and Marty Mortrud for help with iontophoretic virus injections. This work was supported by the Allen Institute for Brain Science. We thank the Allen Institute founder, Paul G. Allen, for his vision, encouragement, and support. Work in the Callaway lab at the Salk Institute was supported by NIH grants EY022577 and MH063912.

REFERENCES

Ahmadlou M, and Heimel JA (2015). Preference for concentric orientations in the mouse superior colliculus. Nat. Commun 6, 6773. [PubMed: 25832803]

Allen AE, Procyk CA, Howarth M, Walmsley L, and Brown TM (2016). Visual input to the mouse lateral posterior and posterior thalamic nuclei: photoreceptive origins and retinotopic order. J. Physiol 594, 1911–1929. [PubMed: 26842995]

Baldwin MKL, Wong P, Reed JL, and Kaas JH (2011). Superior colliculus connections with visual thalamus in gray squirrels (Sciurus carolinensis): evidence for four subdivisions within the pulvinar complex. J. Comp. Neurol 519, 1071–1094. [PubMed: 21344403]

Baldwin MKL, Balaram P, and Kaas JH (2013). Projections of the superior colliculus to the pulvinarin prosimian galagos (Otolemur garnettii) and VGLUT2 staining of the visual pulvinar. J. Comp. Neurol 521, 1664–1682. [PubMed: 23124867]

Baldwin MKL, Balaram P, and Kaas JH (2017). The evolution and functions of nuclei of the visual pulvinar in primates. J. Comp. Neurol 525, 3207–3226. [PubMed: 28653446]

Beltramo R, and Scanziani M (2019). A collicular visual cortex: neocortical space for an ancient midbrain visual structure. Science 363, 64–69. [PubMed: 30606842]

Bender DB (1983). Visual activation of neurons in the primate pulvinar depends on cortex but not colliculus. Brain Res. 279, 258–261. [PubMed: 6640346]

Berman RA, and Wurtz RH (2010). Functional identification of a pulvinar path from superior colliculus to cortical area MT. J. Neurosci 30, 6342–6354. [PubMed: 20445060]

Berman RA, and Wurtz RH (2011). Signals conveyed in the pulvinar pathway from superior colliculus to cortical area MT. J. Neurosci 31, 373–384. [PubMed: 21228149]

Berman RA, Cavanaugh J, McAlonan K, and Wurtz RH (2017). A circuit for saccadic suppression in the primate brain. J. Neurophysiol 117, 1720–1735. [PubMed: 28003409]

Butler AB (2008). Evolution of the thalamus: a morphological and functional review. Thalamus Relat. Syst 4, 35–58.

Casanova C, and Molotchnikoff S (1990). Influence of the superior colliculus on visual responses of cells in the rabbit's lateral posterior nucleus. Exp. Brain Res 80, 387–396. [PubMed: 2358052]

Chomsung RD, Petry HM, and Bickford ME (2008). Ultrastructural examination of diffuse and specific tectopulvinar projections in the tree shrew. J. Comp. Neurol 510, 24–46. [PubMed: 18615501]

Collins DP, Anastasiades PG, Marlin JJ, and Carter AG (2018). Reciprocal circuits linking the prefrontal cortex with dorsal and ventral thalamic nuclei. Neuron 98, 366–379.e4. [PubMed: 29628187]

de Vries SEJ, and Clandinin TR (2012). Loom-sensitive neurons link computation to action in the Drosophila visual system. Curr. Biol 22, 353–362. [PubMed: 22305754]

Dräger UC, and Hubel DH (1975). Responses to visual stimulation and relationship between visual, auditory, and somatosensory inputs in mouse superior colliculus. J. Neurophysiol 38, 690–713. [PubMed: 1127462]

Dräger UC, and Hubel DH (1976). Topography of visual and somatosensory projections to mouse superior colliculus. J. Neurophysiol 39, 91–101. [PubMed: 1249606]

Durand S, Iyer R, Mizuseki K, de Vries S, Mihalas S, and Reid RC (2016).A comparison of visual response properties in the lateral geniculate nucleus and primary visual cortex of awake and anesthetized mice. J. Neurosci 36, 12144–12156. [PubMed: 27903724]

Frost BJ, Cavanagh P, and Morgan B (1988). Deep tectal cells in pigeons respond to kinematograms. J. Comp. Physiol. A Neuroethol. Sens. Neural Behav. Physiol 162, 639–647.

Gabbiani F, Krapp HG, and Laurent G (1999). Computation of object approach by a wide-field, motion-sensitive neuron. J. Neurosci 19, 1122–1141. [PubMed: 9920674]

Gale SD, and Murphy GJ (2014). Distinct representation and distribution of visual information by specific cell types in mouse superficial superior colliculus. J. Neurosci 34, 13458–13471. [PubMed: 25274823]

Gale SD, and Murphy GJ (2016). Active dendritic properties and local inhibitory input enable selectivity for object motion in mouse superior colliculus neurons. J. Neurosci 36, 9111–9123. [PubMed: 27581453]

Gale SD, and Murphy GJ (2018). Distinct cell types in the superficial superior colliculus project to the dorsal lateral geniculate and lateral posterior thalamic nuclei. J. Neurophysiol 120, 1286–1292. [PubMed: 29897837]

Garrett ME, Nauhaus I, Marshel JH, and Callaway EM (2014). Topography and areal organization of mouse visual cortex. J. Neurosci 34, 12587–12600. [PubMed: 25209296]

Gerfen CR, Paletzki R, and Heintz N (2013). GENSAT BAC cre-recombinase driver lines to study the functional organization of cerebral cortical and basal ganglia circuits. Neuron 80, 1368–1383. [PubMed: 24360541]

Groh A, Bokor H, Mease RA, Plattner VM, Hangya B, Stroh A, Deschenes M, and Acsády L (2014). Convergence of cortical and sensory driver inputs on single thalamocortical cells. Cereb. Cortex 24, 3167–3179. [PubMed: 23825316]

Guo ZV, Li N, Huber D, Ophir E, Gutnisky D, Ting JT, Feng G, and Svoboda K (2014). Flow of cortical activity underlying a tactile decision in mice. Neuron 81, 179–194. [PubMed: 24361077]

Guo ZV, Inagaki HK, Daie K, Druckmann S, Gerfen CR, and Svoboda K (2017). Maintenance of persistent activity in a frontal thalamocortical loop. Nature 545, 181–186. [PubMed: 28467817]

Halassa MM, and Kastner S (2017). Thalamic functions in distributed cognitive control. Nat. Neurosci 20, 1669–1679. [PubMed: 29184210]

Harris JA, Mihalas S, Hirokawa KE, Whitesell JD, Knox J, Bernard A, Bohn P, Caldejon S, Casal L, Cho A, et al. (2018). The organization of intracortical connections by layer and cell class in the mouse brain. bioRxiv. 10.1101/292961.

Jun JJ, Steinmetz NA, Siegle JH, Denman DJ, Bauza M, Barbarits B, Lee AK, Anastassiou CA, Andrei A, Aydın Ç, et al. (2017). Fully integrated silicon probes for high-density recording of neural activity. Nature 551, 232–236. [PubMed: 29120427]

Kaas JH, and Lyon DC (2007). Pulvinar contributions to the dorsal and ventral streams of visual processing in primates. Brain Res. Brain Res. Rev 55, 285–296.

Liu Y-J, Wang Q, and Li B (2011). Neuronal responses to looming objects in the superior colliculus of the cat. Brain Behav. Evol 77, 193–205. [PubMed: 21546772]

Lyon DC, Nassi JJ, and Callaway EM (2010). A disynaptic relay from superior colliculus to dorsal stream visual cortex in macaque monkey. Neuron 65, 270–279. [PubMed: 20152132]

Madisen L, Mao T, Koch H, Zhuo JM, Berenyi A, Fujisawa S, Hsu Y-WA, Garcia AJ 3rd, Gu X, Zanella S, et al. (2012). A toolbox of Cre-dependent optogenetic transgenic mice for light-induced activation and silencing. Nat. Neurosci 15, 793–802. [PubMed: 22446880]

Mease RA, Sumser A, Sakmann B, and Groh A (2016). Cortical dependence of whisker responses in posterior medial thalamus in vivo. Cereb. Cortex 26, 3534–3543. [PubMed: 27230219]

Moran PAP (1950). Notes on continuous stochastic phenomena. Biometrika 37, 17–23. [PubMed: 15420245]

Nakamura H, Hioki H, Furuta T, and Kaneko T (2015). Different cortical projections from three subdivisions of the rat lateral posterior thalamic nucleus: a single-neuron tracing study with viral vectors. Eur. J. Neurosci 41, 1294–1310. [PubMed: 25832313]

Oh SW, Harris JA, Ng L, Winslow B, Cain N, Mihalas S, Wang Q, Lau C, Kuan L, Henry AM, et al. (2014). A mesoscale connectome of the mouse brain. Nature 508, 207–214. [PubMed: 24695228]

Pachitariu M, Steinmetz NA, Kadir SN, Carandini M, and Harris KD (2016). Fast and accurate spike sorting of high-channel count probes with KiloSort. Adv. Neural Inf. Process. Syst 29, 4448–4456.

Petersen SE, Robinson DL, and Keys W (1985). Pulvinar nuclei of the behaving rhesus monkey: visual responses and their modulation. J. Neurophysiol 54, 867–886. [PubMed: 4067625]

Purushothaman G, Marion R, Li K, and Casagrande VA (2012). Gating and control of primary visual cortex by pulvinar. Nat. Neurosci 15, 905–912. [PubMed: 22561455]

Rossant C, Kadir SN, Goodman DFM, Schulman J, Hunter MLD, Saleem AB, Grosmark A, Belluscio M, Denfield GH, Ecker AS, et al. (2016). Spike sorting for large, dense electrode arrays. Nat. Neurosci 19, 634–641. [PubMed: 26974951]

Roth MM, Dahmen JC, Muir DR, Imhof F, Martini FJ, and Hofer SB (2016). Thalamic nuclei convey diverse contextual information to layer 1 of visual cortex. Nat. Neurosci 19, 299–307. [PubMed: 26691828]

Saalmann YB, Pinsk MA, Wang L, Li X, and Kastner S (2012). The pulvinar regulates information transmission between cortical areas based on attention demands. Science 337, 753–756. [PubMed: 22879517]

Schmitt LI, Wimmer RD, Nakajima M, Happ M, Mofakham S, and Halassa MM (2017). Thalamic amplification of cortical connectivity sustains attentional control. Nature 545, 219–223. [PubMed: 28467827]

Shang C, Chen Z, Liu A, Li Y, Zhang J, Qu B, Yan F, Zhang Y, Liu W, Liu Z, et al. (2018). Divergent midbrain circuits orchestrate escape and freezing responses to looming stimuli in mice. Nat. Commun 9, 1232. [PubMed: 29581428]

Sherman SM (2016). Thalamus plays a central role in ongoing cortical functioning. Nat. Neurosci. 19, 533–541. [PubMed: 27021938]

Shipp S (2003). The functional logic of cortico-pulvinar connections. Philos. Trans. R. Soc. Lond. B Biol. Sci 358, 1605–1624. [PubMed: 14561322]

Siegle JH, López AC, Patel YA, Abramov K, Ohayon S, and Voigts J (2017). Open Ephys: an open-source, plugin-based platform for multichannel electrophysiology. J. Neural Eng 14, 045003. [PubMed: 28169219]

Sun H, and Frost BJ (1998). Computation of different optical variables of looming objects in pigeon nucleus rotundus neurons. Nat. Neurosci 1, 296–303. [PubMed: 10195163]

Takahashi T (1985). The organization of the lateral thalamus of the hooded rat. J. Comp. Neurol 231, 281–309. [PubMed: 3968240]

Tohmi M, Meguro R, Tsukano H, Hishida R, and Shibuki K (2014). The extrageniculate visual pathway generates distinct response properties in the higher visual areas of mice. Curr. Biol 24, 587–597. [PubMed: 24583013]

Wang Q, and Burkhalter A (2013). Stream-related preferences of inputs to the superior colliculus from areas of dorsal and ventral streams of mouse visual cortex. J. Neurosci 33, 1696–1705. [PubMed: 23345242]

Wang Q, Sporns O, and Burkhalter A (2012). Network analysis of cortico-cortical connections reveals ventral and dorsal processing streams in mouse visual cortex. J. Neurosci 32, 4386–4399. [PubMed: 22457489]

Wei P, Liu N, Zhang Z, Liu X, Tang Y, He X, Wu B, Zhou Z, Liu Y, Li J, et al. (2015). Processing of visually evoked innate fear by a non-canonical thalamic pathway. Nat. Commun 6, 6756. [PubMed: 25854147]

Wickersham IR, Lyon DC, Barnard RJO, Mori T, Finke S, Conzelmann K-K, Young JAT, and Callaway EM (2007). Monosynaptic restriction of transsynaptic tracing from single, genetically targeted neurons. Neuron 53, 639–647. [PubMed: 17329205]

Zhao S, Ting JT, Atallah HE, Qiu L, Tan J, Gloss B, Augustine GJ, Deisseroth K, Luo M, Graybiel AM, and Feng G (2011). Cell type–specific channelrhodopsin-2 transgenic mice for optogenetic dissection of neural circuitry function. Nat. Methods 8, 745–752. [PubMed: 21985008]

Zhao X, Liu M, and Cang J (2014). Visual cortex modulates the magnitude but not the selectivity of looming-evoked responses in the superior colliculus of awake mice. Neuron 84, 202–213. [PubMed: 25220812]

Zhou H, Schafer RJ, and Desimone R (2016). Pulvinar-cortex interactions in vision and attention. Neuron 89, 209–220. [PubMed: 26748092]

Zhou NA, Maire PS, Masterson SP, and Bickford ME (2017). The mouse pulvinar nucleus: organization of the tectorecipient zones. Vis. Neurosci 34, E011. [PubMed: 28965504]

Zhuang J, Ng L, Williams D, Valley M, Li Y, Garrett M, and Waters J (2017). An extended retinotopic map of mouse cortex. eLife 6, e18372. [PubMed: 28059700]

Highlights

- Mouse pulvinar (LP) contains 3 anatomically and functionally defined subregions
- Anterior LP (aLP) and posterior LP (pLP) contain separate maps of visual space
- V1 drives aLP; superior colliculus (SC) drives responses to object motion in pLP
- The SC-pLP pathway is most strongly connected with ventral stream cortical areas

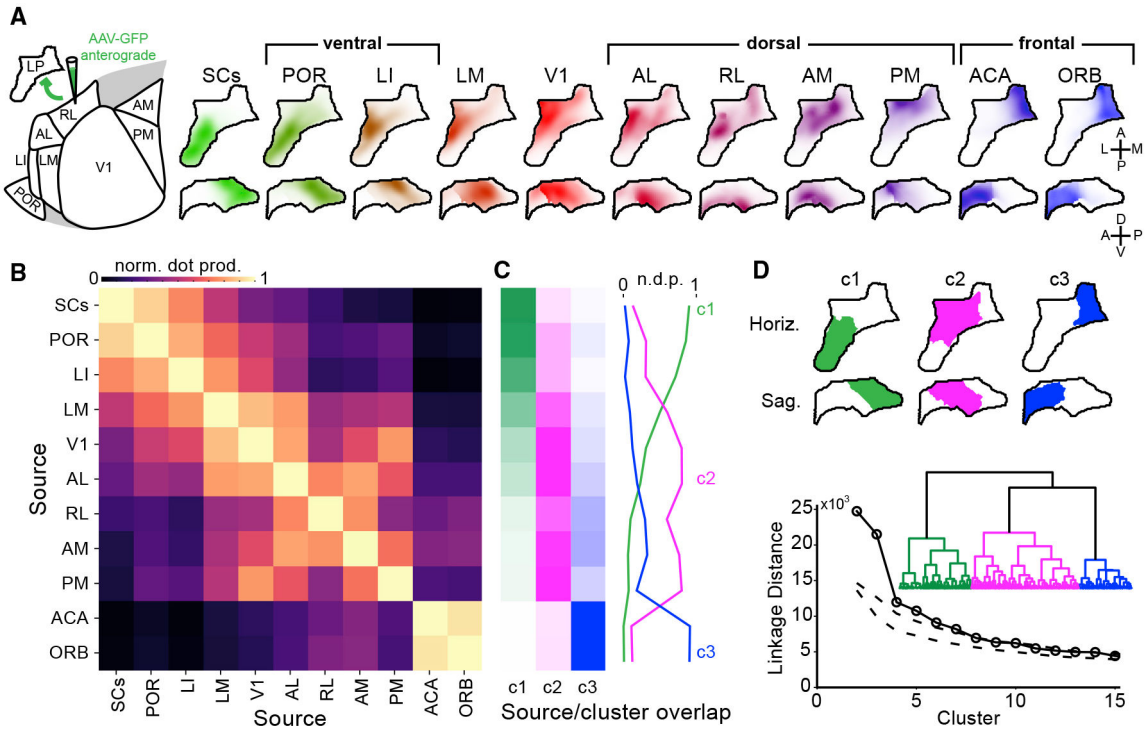

Figure 1. Input Connectivity Reveals Three Broad LP Subregions

(A) Left: schematic of input mapping experiments, showing visual cortical areas in the horizontal plane. Right: location of anterogradely labeled axons in LP from various cortical and subcortical input sources. Input volumes are shown as horizontal (top row) and sagittal projections (bottom row) and represent average fluorescence across multiple tracer injection experiments registered in the Allen Mouse Common Coordinate Framework (STAR Methods).

(B) Overlap of inputs to LP from different sources (normalized voxel-wise dot product).

(C) Overlap of input from each source with clusters of LP voxels based on all inputs (hierarchical clustering using Ward's linkage criterion).

(D) Top: projections of LP voxels belonging to the first three clusters. Bottom: dendrogram (inset) showing linkage distance of LP voxels based on anatomical inputs. Linkage distances for the first 15 clusters are compared with clusters formed from random shuffling of data across voxels for each input source (dashed lines; 1%–99% confidence interval).

SCs, superficial superior colliculus; POR, postrhinal area; LI, laterointermediate area; LM, lateromedial area; V1, primary visual cortex; AL, anterolateral area; RL, rostrolateral area; AM, anteromedial area; PM, posteromedial area; ACA, anterior cingulate; ORB, orbital cortex.

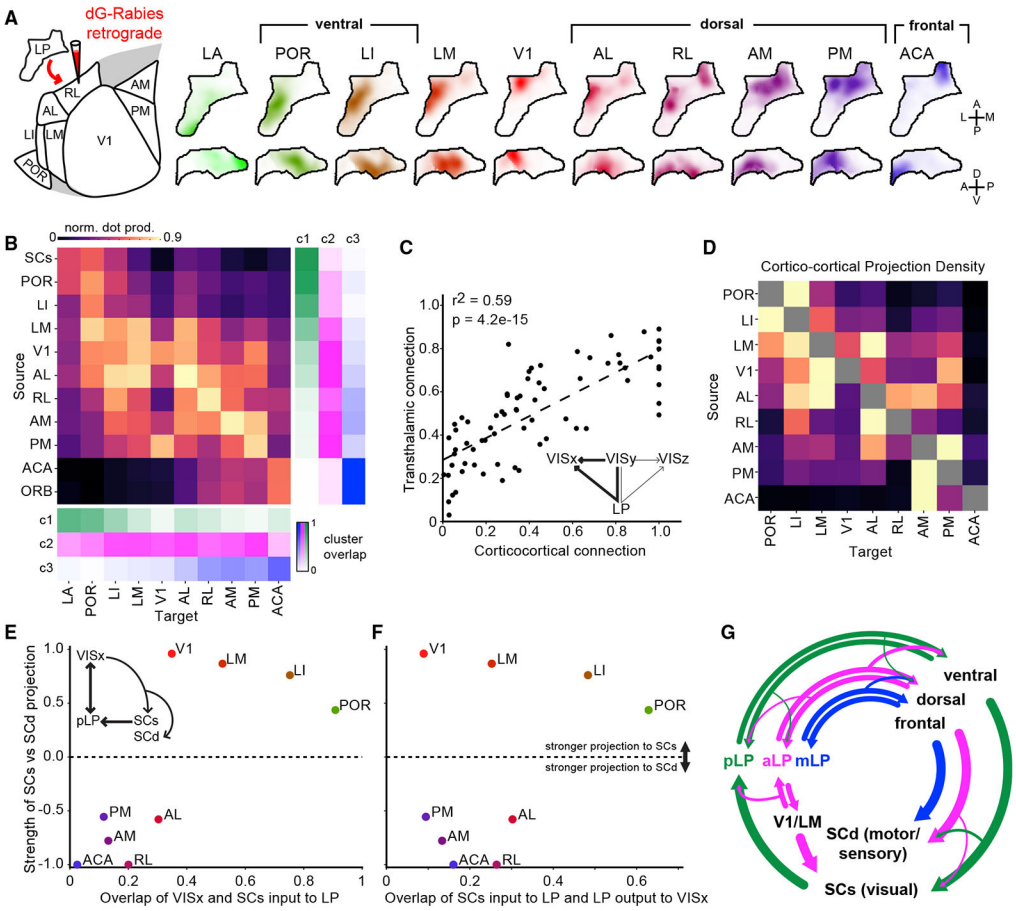

Figure 2. LP Input-Output Mapping Reveals Reciprocal and Relay Transthalamic Pathways

(A) Location of retrogradely labeled cells in LP following rabies injections in various output targets. Output volumes are shown as horizontal and sagittal projections as for the input volumes shown in Figure 1A.

(B) Overlap (normalized dot product) in LP of input and output volumesfor each source-target region pair. Right: the overlap of input volumes and clusters from Figure 1C are shown here again for reference. Bottom: overlap of output volumes and the clusters from Figure 1.

(C and D) Comparison of direct cortico-cortical and indirect cortico-LP-cortical (transthalamic) connectivity. The density of axons directly connecting visual cortical areas (D; cortico-cortical connections, row-normalized) are compared in (C) to the overlap of input from and output to the same source-target pairs in LP (B; putative transthalamic connections). p value from two-sided Wald test for significant correlation.

(E) Relative strength of cortical projections to SCs or deep superior colliculus (SCd) as a function of overlap between cortical and SCs LP projections for nine cortical areas (x axis taken from the top row of Figure 1B).

(F) The same as (E) but for overlap of SCs input and LP output to the same cortical areas (x axis taken from the top row of B).

Values on the y axis for (E) and (F) are the difference of the projection density to SCs and SCd divided by their sum (STAR Methods).

(G) Diagram summarizing connectivity between LP, cortex, and SC.

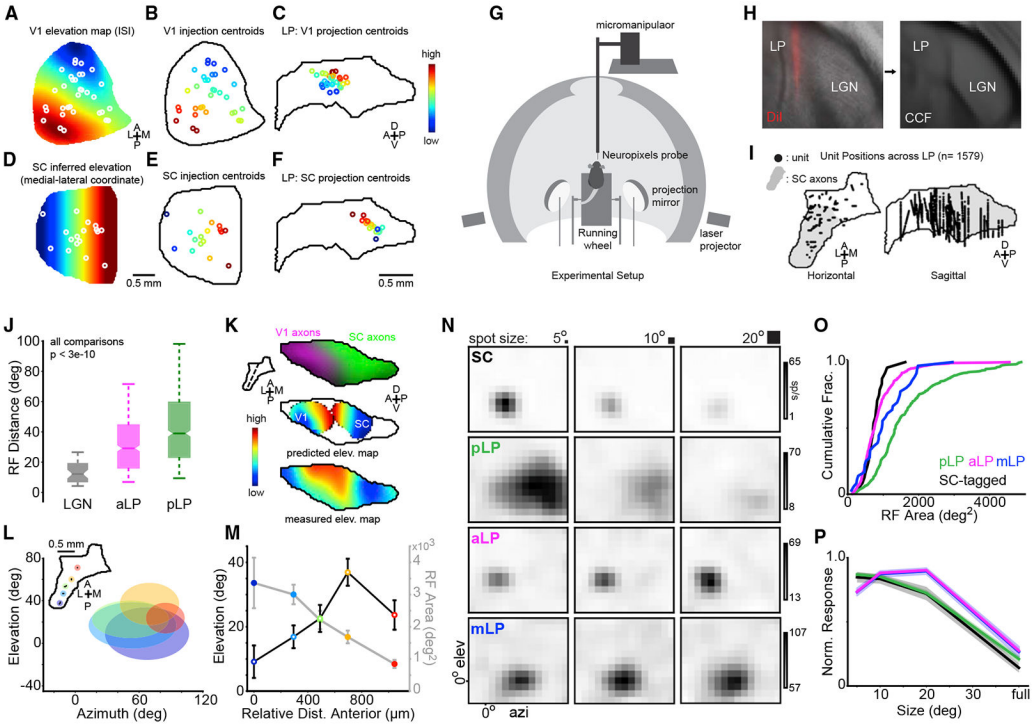

Figure 3. Posterior and Anterior LP Have Separate Maps of Visual Space and Distinct Receptive Field Properties

(A) Mean intrinsic signal imaging (ISI) elevation map for V1, with the location of V1 injections from the Allen Connectivity Database superimposed (white circles indicate injection centroids).

(B) V1 injections colored by assigned elevation according to the map in (A).

(C) V1 projection centroids in LP (sagittal plane) for injections in (B), colored by assigned elevation. These centroids were smoothed to create the V1 predicted elevation map in (K).

(D–F) The same as (A)–(C) for SC injections. Elevation in SC is inferred from the medial-lateral coordinate (STAR Methods).

(D) Elevation map in SC inferred from the medial-lateral coordinate (STAR Methods).

(E) SC infection centroids as in (B).

(F) SC projection centroids in LP.

(G) Diagram of the experimental setup for visual stimulation and neural recording.

(H) DiI labeling of the probe tract recovered from *post hoc* histology and registered to the CCF.

(I) Recording locations for all LP neurons displayed on horizontal and sagittal projections of LP. The gray region denotes the SC-recipient LP.

(J) Receptive field distance for pairs of cells separated by 20 μm or less in dLGN (gray, n = 48 pairs), aLP (magenta, n = 350 pairs), or pLP (green, n = 554 pairs). Only cells from the same probe insertion were compared. Box edges indicate first and third quartiles. A notch indicates 95% confidence interval (CI) for the median (band). Whiskers denote 5th and 95th percentiles. Wilcoxon rank-sum test.

(K) Top: LP slice showing SC (green) and V1 (magenta) input to LP. The plane of the slice is indicated by the dotted line in the inset. Center: predicted LP elevation map based on

anatomical V1 input (left) or SC input (right). Bottom: composite elevation map for all LP cells.

(L) Data from an experiment in which five insertions were made serially in one mouse. Recording locations for each insertion are shown in the inset. Ellipses are centered at the mean RF center for each insertion (color-coded to match the inset). The ellipse shape reflects the mean RF shape for neurons at each location.

(M) Mean receptive field area (closed circles) and elevation (open circles) for each recording location in (L). Colors are as in (L). Error bars represent SE.

(N) Off receptive fields for example SC (optotagged), pLP, aLP, and mLP neurons (rows). Receptive fields were mapped with sparse noise consisting of 5°, 10°, and 20° squares (columns).

(O and P) Cumulative distribution of receptive field area (O) and mean size tuning (P) for SC (black), pLP (green), aLP (magenta), and mLP (blue) neurons. Shaded regions in (P) denote SE.

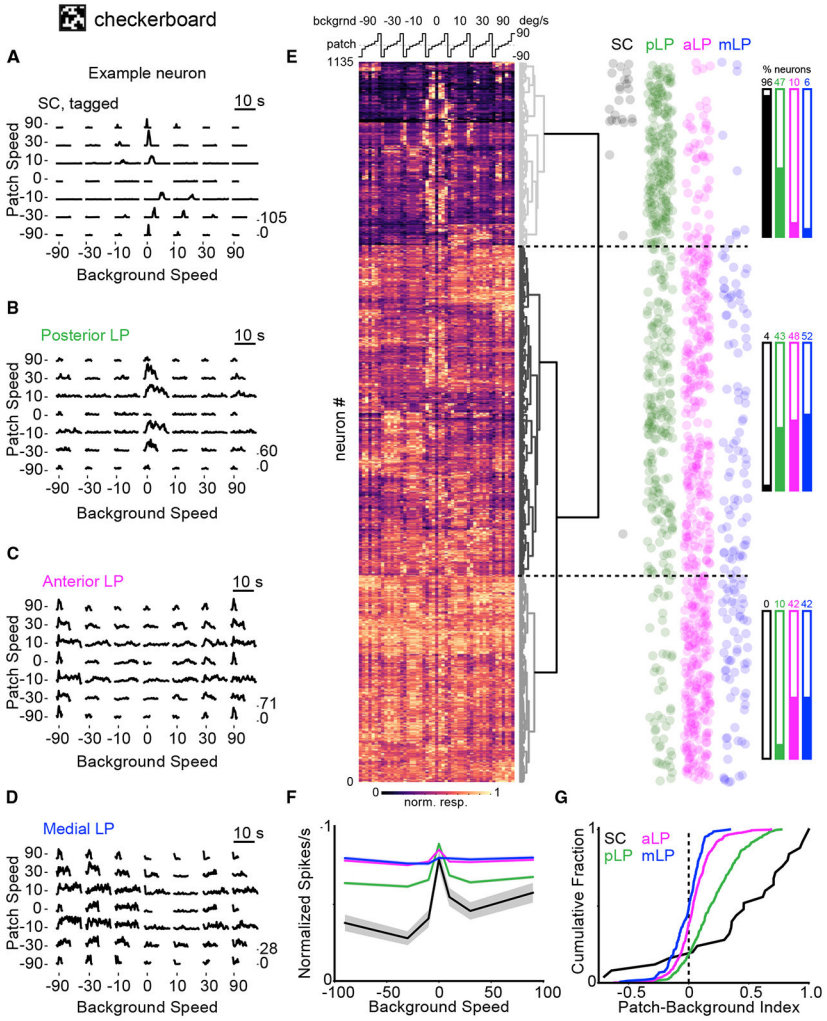

Figure 4. LP Neurons Differ in Their Response to Object and Background Motion

(A) Spike density functions of an example optotagged SC neuron (left) and mean population response (right) to a random checkerboard background (full field) and patches (10°) moving relative to each other at various speeds (positive speeds are nasal to temporal). Checkerboard squares are 1°. Patch speed 0°/s trials are background motion only. Background 0°/s trials consist of patches moving over a stationary random checkerboard background. Because the texture of patches and background are indistinguishable, patches moving with the same speed and direction as the background are invisible (equivalent to patch speed 0°/s trials).

(B–D) The same as (A) for pLP (B), aLP (C), and mLP (D) neurons.

(E) Left: heatmap showing the normalized response of all SC and LP neurons to the checkerboard stimulus. Each row represents one cell. The matrix of 7 patch and 7 background speeds shown in (A–D) is linearized to a 49-element vector, as shown above the heatmap. Hierarchical clustering was used to order the rows according to the linkage distance between cells (represented by the dendrogram to the right of the heatmap). Right: dot plots showing the position (row) of each cell from an SC or an LP subregion along the heatmap. The horizontal locations of the dots were jittered randomly to reduce overlap. Bar

plots indicate the percentage of cells from each region belonging to the three main clusters in the heatmap data.

(F) Population tuning curves for background speed (normalized column max of the checkerboard response matrix) for the SC (black), pLP (green), aLP (magenta), and mLP (blue). Shaded regions indicate standard error.

(G) Cumulative distributions of patch-background index values for SC, pLP, aLP, and mLP in response to the checkerboard stimulus. The patch-background index is the difference between the maximum responses to patch (background speed 0°/s) and background (patch speed 0°/s) motion divided by their sum.

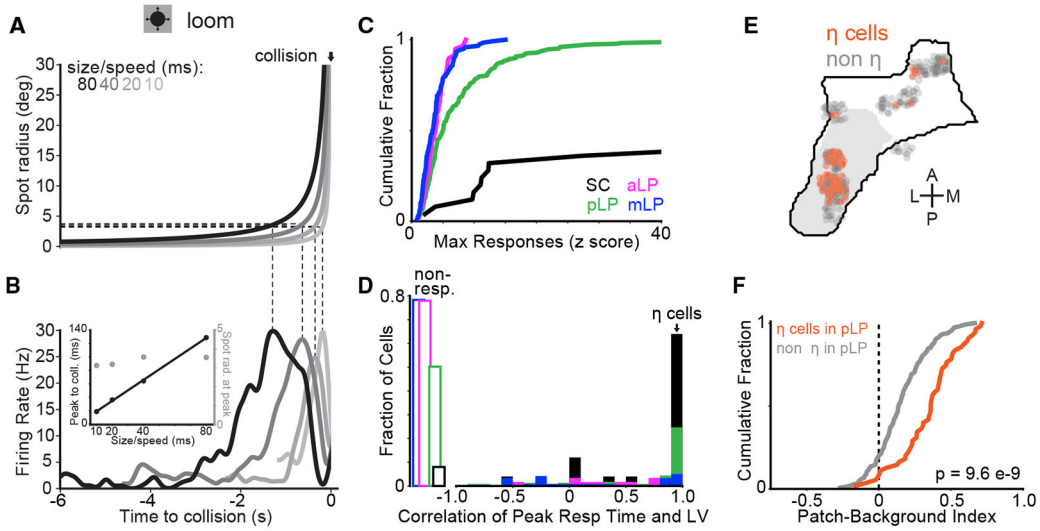

Figure 5. SC and Posterior LP Neurons Respond More Strongly to Looming Stimuli

(A) Trajectory of the spot radius for looming stimuli at four size-to-speed ratios.

(B) Firing rate of an example neuron in posterior LP to looming stimuli depicted in (A). Dotted lines relate spot radius to time of peak firing rate. Inset: time of peak firing rate relative to collision plotted against size-to-speed ratio for the example neuron in (B) (filled black circles, left axis) and spot radius at peak firing rate plotted against size-to-speed ratio for the same neuron (open gray circles, right axis).

(C) Cumulative distribution of max loom response (*Z* score) across all conditions for neurons in SC (black), pLP (green), aLP (magenta), and mLP (blue). Note that, because of their low spontaneous firing rates, many SC neurons had *Z* scores greater than 40.

(D) Histogram of correlation between peak response time and size-to-speed ratio for cells in SC and LP subregions (colors as in C). Cells with a correlation value greater than 0.9 were classified as η-type. Open rectangles on the left represent a fraction of cells that were not responsive to looming stimuli.

(E) Location of η cells shown in a horizontal projection of LP. The gray region denotes SC-recipient LP.

(F) Cumulative distribution of checkerboard patch-background index values for η (orange, n = 55 cells) and non-η (gray, n = 150 cells) neurons in posterior LP; Wilcoxon rank-sum test.

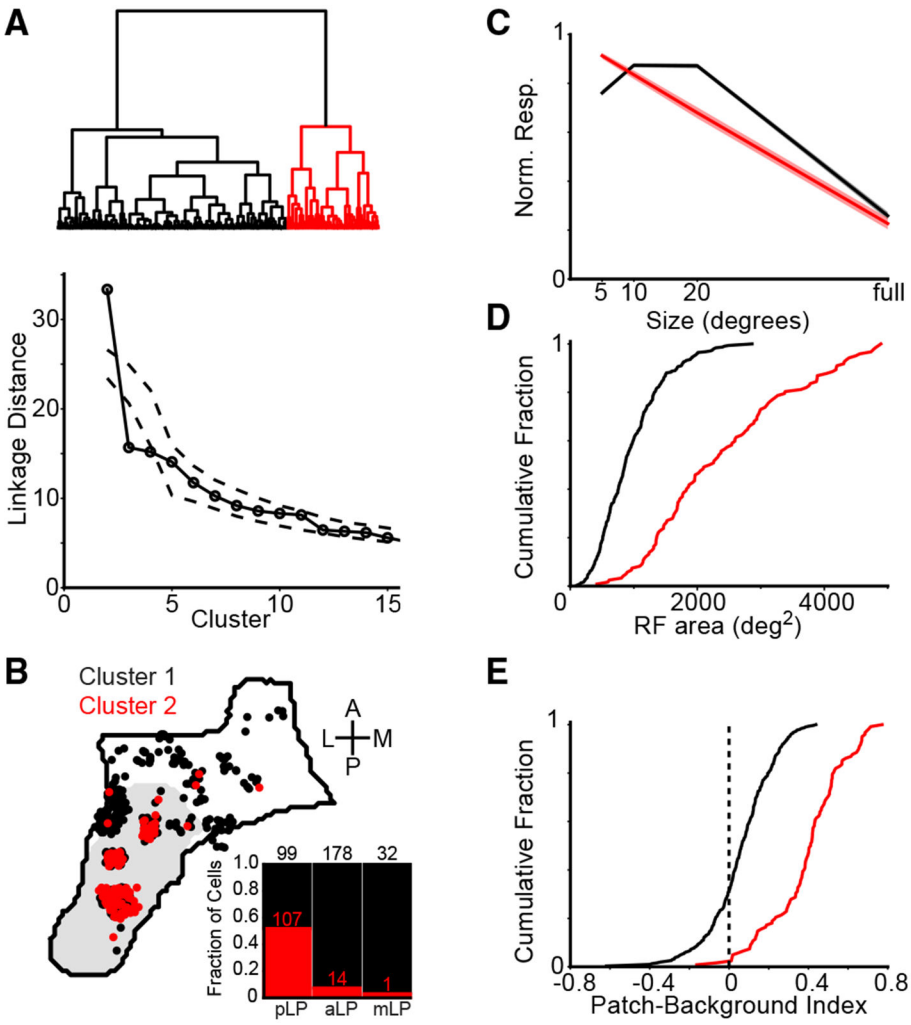

Figure 6. Visual Response Properties Reveal Functional-Anatomical Segregation in LP

(A) Top: dendrogram representing hierarchical clustering (Ward's linkage criterion) of LP neurons based on visual response properties. Bottom: linkage distance for the first 15 clusters compared with clusters formed from the same data randomly shuffled across neurons for each visual response parameter (dashed lines are 1%–99% confidence interval).

(B) Horizontal projection of the location in LP of neurons from each cluster. Inset: stacked bar plot showing the fraction of cells in each cluster across LP subregions (the numbers give the total cell count in each bar).

(C–E) Mean size tuning (C) and cumulative distributions of receptive field area (D) and patch-background index (E) for the two clusters.

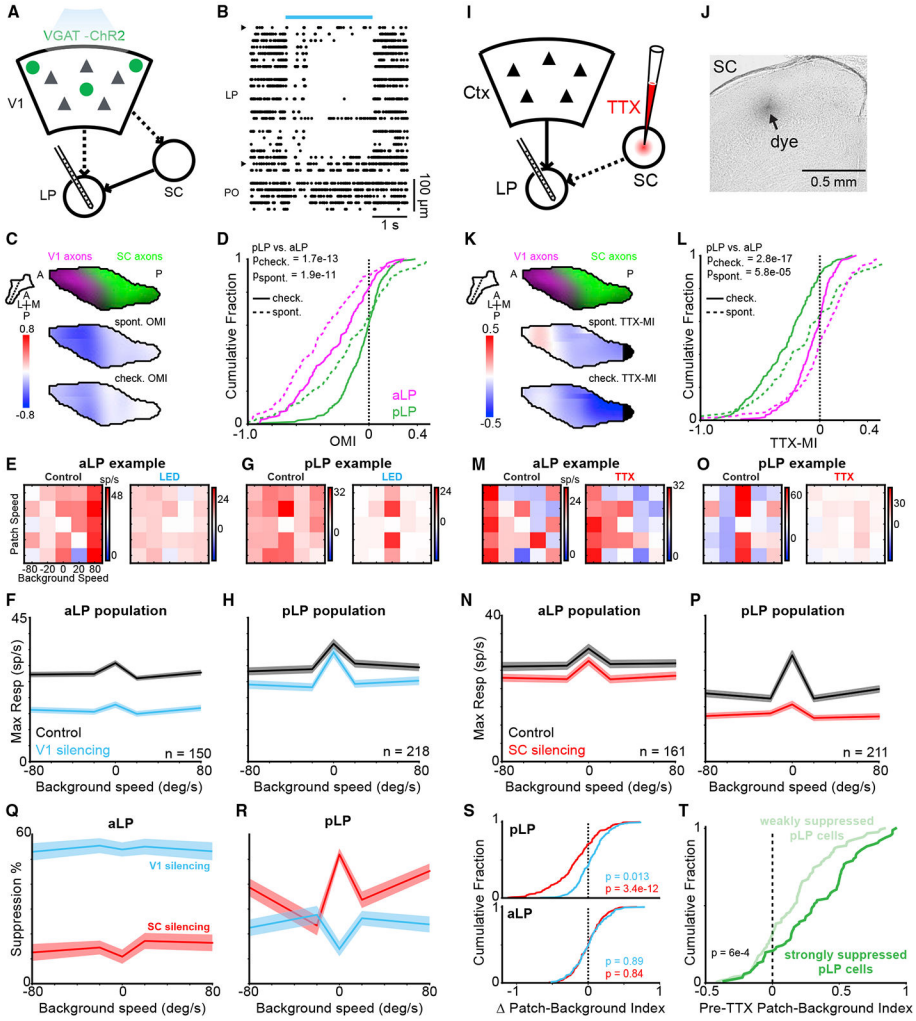

Figure 7. V1 and SC Silencing Have Divergent Effects on Activity in Anterior and Posterior LP

(A) V1 silencing was accomplished by transcranial illumination of the cortex with blue light in VGAT-ChR2 mice. Recordings were performed simultaneously in LP.

(B) Raster plot showing spontaneous activity of all thalamic units for one silencing trial. A blue bar indicates light delivery. Units are ordered by dorsal-ventral position. Carets demarcate LP boundaries. Units ventral of LP are in the posterior thalamic nucleus (PO).

(C) Top: LP slice showing SC (green) and V1 (magenta) input to LP. The plane of the slice is indicated by a dotted line in the inset. Center: optogenetic modulation index (OMI) for spontaneous activity averaged across all units in LP. The OMI is defined as (optogenetic firing rate − control firing rate)/(optogenetic firing rate + control firing rate). Bottom: OMI for the checkerboard response.

(D) Cumulative distribution of the OMI for neurons in pLP (green, n = 218 cells) and aLP (magenta, n = 150 cells) during spontaneous activity (dotted lines) and the checkerboard stimulus (solid lines). The p values compare pLP with aLP; Wilcoxon rank-sum test.

(E) Example patch-checkerboard matrix for an aLP neuron during control (left) and V1 silencing (right) trials.

(F) Mean background speed tuning during control (black) and V1 silencing (blue) for aLP population. Values are maximum projections along the columns of the checkerboard response matrix averaged across cells. Shaded regions denote the SEM.
(G and H) Same as (E) and (F) but for pLP.
(I) SC silencing was accomplished by injecting TTX into SC while recording in LP (n = 211 pLP cells, 161 aLP cells).
(J) Bright-field image confirming the deposition of dye in sSC after a TTX injection.
(K–P) As in (C–H) for SC silencing.
(K) Map of TTX-MI in LP.
(L) Cumulative distribution of TTX-MI values.
(M) Responses of an example aLP neuron during control (left) and SC silencing (right) trials.
(N) Mean background speed tuning during control (black) and SC silencing (red) for the aLP population.
(O and P) same as (E) and (F) but for pLP.
(Q) Suppression as a function of checkerboard background speed for aLP population during cortical (blue) and SC (red) silencing.
(R) As in (Q) for the pLP.
(S) Change in the patch-background index during cortical and SC silencing for pLP (top) and aLP (bottom). A negative shift indicates a reduction in patch preference. Wilcoxon signed-rank test for shift from zero.
(T) Distribution of patch-background index values (before TTX injection in the SC) of pLP neurons that were strongly (TTX-MI < −0.33, n = 86 cells) or weakly (TTX-MI > −0.33, n = 125 cells) inhibited by SC inactivation. Wilcoxon rank-sum test.

Table 1.

Number of Cells Recorded during Electrophysiology Experiments

	SC		pLP	aLP	mLP	dLGN
	Optotagged	**Non-tagged**				
Sparse noise	24/25 (96%)	75/97 (77%)	364/633 (58%)	306/751 (41%)	36/195 (18%)	42/64 (66%)
Gratings	22/25 (88%)	72/97 (74%)	353/494 (71%)	312/598 (52%)	105/195 (54%)	24/46 (52%)
Checkerboard	25/25 (100%)	82/97 (85%)	440/499 (88%)	519/640 (81%)	151/195 (77%)	60/64 (94%)
Loom	23/25 (92%)	59/97 (61%)	113/227 (50%)	13/59 (22%)	26/120 (22%)	–
V1 inactivation (checkerboard)	–	268/292 (92%)	218/266 (82%)	150/236 (64%)	–	–
SC inactivation (checkerboard)	–	–	211/243 (87%)	161/217 (74%)	–	–

Values indicate the fraction of cells that responded (STAR Methods) to each of the visual stimulus types shown in the left column or to the checkerboard stimulus for V1 and SC inactivation experiments. For the sparse noise stimulus, a spatial receptive field that could be fit to a two-dimensional Gaussian was also required to include a cell in the numerator. Only a subset of the stimuli was presented during some experiments. SC optotagging experiments were performed with Ntsr1-GN209 Cre x Ai32 mice. Cortical inactivation experiments were performed with VGAT-ChR2 mice. The numbers of mice used for control experiments were 5 (SC), 30 (LP), and 3 (dLGN); 5 (SC) and 6 (LP) for V1 inactivation; and 8 (LP) for SC inactivation. In some cases, we recorded twice from the same mouse on consecutive days. The numbers of recording sessions for control experiments were 8 (SC), 50 (LP), and 3 (dLGN); 9 (SC) and 11 (LP) for V1 inactivation; and 10 (LP) for SC inactivation.

KEY RESOURCES TABLE

REAGENT or RESOURCE	SOURCE	IDENTIFIER
Bacterial and Virus Strains		
AAV1 CAG FLEX GFP	Penn Vector Core	Addgene 51502
AAV1 CAG FLEX tdTomato	Penn Vector Core	Addgene 51503
Rabies SADΔG-GFP	Wickersham et al., 2007	N/A
Rabies SADΔG-mCherry	Wickersham et al., 2007	N/A
Chemicals, Peptides, and Recombinant Proteins		
Tetrodotoxin (TTX)	Hello Bio	HB1035
Evans Blue	Sigma	E2129
Experimental Models: Organisms/Strains		
Mouse: C57BL/6J	The Jackson Laboratory	JAX: 000664
Mouse: Ntsr1-GN209 Cre	GENSAT	030780-UCD
Mouse: Ai32	The Jackson Laboratory	JAX: 024109
Mouse: VGAT-ChR2-eYFP	The Jackson Laboratory	JAX: 014548
Software and Algorithms		
Open Ephys GUI	Siegle et al., 2017	https://github.com/open-ephys/plugin-GUI
Kilosort	Pachitariu et al., 2016	https://github.com/cortex-lab/KiloSort
phy	Rossant et al., 2016	https://github.com/kwikteam/phy